

Supple Graphene Bio-Platform for point-of-care early detection and monitoring of Alzheimer's Disease

# D2.3 Conjugated MNPs/Aptamers Binding to AD Biomarkers evaluation, Version 1

**AUTh** 

04/04/2025





#### **Document Information**

Issued by:	AUTh
Issue date:	04/04/2025
Due date:	31/03/2025
Work package leader:	AUTh
Dissemination level:	PU

#### **Document History**

Version	Date	Modifications made by
0.1	01/03/2025	Table of Contents provided by AUTh
0.2	17/03/2025	First draft with input from partners circulated by AUTh
0.3	25/03/2025	Final draft circulated for Review by AUTh
0.4	31/03/2025	Quality Review by Q-PLAN
0.5	02/04/2025	Quality Review by GRAPHEAL
1.0	04/04/2025	Final version for submission
1.1	26/09/2025	Modified version prepared by Novaptech

#### **Authors**

Name(s)	Beneficiary
M. Angelakeris, A. Pantazaki	AUTh
J.J. Toulmé, S. Kumar	Novaptech
C. Bosch, P. Goktas	CeADAR

In case you want any additional information, or you want to consult with the authors of this document, please send your inquiries to: <a href="mailto:tsolakis@qplan-intl.gr">tsolakis@qplan-intl.gr</a>

#### **Quality Reviewers**

Name(s)	Beneficiary
A. Folas, A. Tsolakis	Q-PLAN
V. Bouchiat	GRAPHEAL

#### Disclaimer

Funded by the European Union under GA no. 101120706. Views and opinions expressed are however those of the authors only and do not necessarily reflect those of the European Union or CNECT. Neither the European Union nor the granting authority can be held responsible for them.

#### © 2D-BioPAD Consortium, 2023 - 2027

Reproduction is authorised provided the source is acknowledged.



## List of Terms and Definitions

Abbreviation	Definition	Abbreviation	Definition
Αβ	Amyloid Beta	IPR	Intellectual Property Rights
AD	Alzheimer's Disease	IVD	In-Vitro Diagnostics
ADNI	Alzheimer's Disease Neuroimaging Initiative	IVDR	In-Vitro Diagnostics Regulation
Al	Artificial Intelligence	KER	Key Exploitable Result
APOE	Apolipoprotein E gene	LFA	Lateral-flow biosensor assays
"ATN"	Research framework which covers amyloid abnormalities ('A'), tau protein changes ('T'), and evidence of neurodegeneration ('N'), irrespective of clinical phenotypes	LMICs	Low-and middle-income countries
BBBM	Blood-based Biomarker	LOD	Limit of Detection
BRU	Brain Research Unit at UEF	MCI	Mild Cognitive Impairment
CIS	Clinical Information System	MDR	Medical Device Regulation
CSF	Cerebrospinal fluid	MNPs	Magnetic Nanoparticles
D	Deliverable	MRI	Magnetic Resonance Imaging
DFT	Density-functional theory	NACC	National Alzheimer's Coordinating Center
DMP	Data Management Plan	NFL	Neurofilament Light
DNA	Deoxyribonucleic acid	NIA-AA	National Institute on Aging and Alzheimer's Association
DNS	Digital Neuro Signature	NPs	Nanoparticles
EC	European Commission	NTA-tau	N-terminal containing tau fragments
ECR	Ethical Consideration Roadmap	PCR	Polymerase chain reaction
EDC	Electronic Data Capture	PDB	Protein Data Bank
ELISA	Enzyme-linked immunosorbent assay	PET	Positron emission tomography
ePADs	Electrochemical paper-based analytical devices	PhD	Philosophy Doctorate
ESC	Ethics Steering Committee	PoC	Point-of-Care
EU	European Union	Post-Doc	Post Doctoral
FAIR	Findable, Accessible, Interoperable and Re-usable	PPIE	Patient and Public Involvement and Engagement
FDG	Fluorodeoxyglucose	RNA	Ribonucleic acid
FG	Fluorographene	QA	Quality Assurance
GAAIN	Global Alzheimer's Association Interactive Network	QC	Quality Control
GCP	Good Clinical Practice	QoL	Quality of Life
GDPR	General Data Protection Regulation	RWE	Real World Evidence
GFAP	Glial Fibrillary Acidic Protein	SELEX	Systematic Evolution of Ligands by Exponential Enrichment
GFET	Graphene field effect transistor	SCI	Subjective Cognitive Impairment
GGC	Greenlight Guru Clinical	SOP	Standard operating procedure
GMP	Good Manufacturing Practice	sTREM2	Soluble triggering receptor expressed on myeloid cells 2
GP	General practitioner	tau	Tau protein
HCPs	Healthcare Professionals/Practitioners	TDP-43	TAR DNA-binding protein 43
HICs	High-income countries	WMA	World Medical Association
hPSCreg	Human Pluripotent Stem Cell Registry	WP	Work Package



## **Table of Contents**

Executive Summary	4
1. Introduction	5
2D-BioPAD Approach	5
WP2: Biomarkers Binding: Quantitative Analysis	8
2. Aptamers' Identification	10
3. Aptamers' Optimization	35
4. Nanoparticles' Design & Synthesis	39
5. Conjugation of MNPs with Aptamers and Biomarkers	45
6. Next Steps & Critical Milestones	52
Appendix I: Amyloid beta and monomerization protocol	54
Appendix II: pTau-217 sequence under study	55
Appendix III: Protocol for MNPs/aptamer conjugation	57



This report, outlines the activities and findings related to Conjugated MNPs/Aptamers Binding to AD Biomarkers evaluation, Version 1 which corresponds to WP2 named Biomarkers Binding: Quantitative Analysis. The goal of WP2 is to provide standardized nano-based probes for reliable, efficient, and diagnosis of AD and includes three major areas with specific tasks and milestones:

**AD biomarker Aptamers:** Identification, synthesis, evaluation, optimization

**Magnetic nanoparticles:** Synthesis and characterization of magnetic nanoparticles as carriers and enablers and

**Conjugation processes**: Immobilization, Functionalization and Evaluation of Conjugated MNPs/Aptamers/Biomarkers.

Within this reporting period, the focus is on certain DNA aptamers for specific AD protein biomarkers, namely five different AD biomarker proteins viz. A $\beta$ 40, A $\beta$ 42, NFL, GFAP and p-tau 217, as defined and explained in D1.2 Architecture and System Design.<sup>1</sup>

An AI framework assists the experimental effort by narrowing down how to translate the indicative aptamers to contribute to a better experimental development, following literature model metrics. We currently evaluating protein sequences to identify promising aptamer candidates with good interaction scores and validate them experimentally.

**Aß40** and **Aß42**: We are currently examining the conjugation of commercially available aptamers: for A $\beta$ 40, RNV95 and A $\beta$ 7-92-1H1. Conjugation efficiency of these aptamers with the synthesized MNPs and amyloid peptides is underway with the involvement of sophisticated immunological techniques (Western blotting, commercial ELISA kits, Dot blotting).

**NFL:** Full-length aptamers identified for Nfl will be truncated; to limit the cross-reactivity of the currently identified aptamers, truncation approach will be decided on selective and sequential removal of sequence portions.

**GFAP:** High affinity aptamers have been selected against GFAP and truncation of these aptamers has generated short and specific GFAP aptamers. These aptamers are now being conjugated to nanoparticles.

**pTau217:** Aptamer selection is currently undergoing against small peptides covering the region of interest on protein. Once the selection is completed, the candidates obtained will be tested rigorously for binding with pTau-217 protein.

MNPs: core-shell Fe<sub>3</sub>O<sub>4</sub>/Au magnetic nanoparticles are routinely synthesized and conjugated with validated protocol with corresponding aptamers. So far TBA and A $\beta$ 40 and A $\beta$ 42 are effectively conjugated with MNPs. All specimens, once effectively conjugation of MNPs with aptamers is achieved, are progressing in examining binding efficiency with biomarkers.

.

<sup>&</sup>lt;sup>1</sup> D1.2 was submitted on 2<sup>nd</sup> July2024.



#### 2D-BioPAD Approach

The investigation carried out in the framework of 2D-BioPAD demonstrated that the situation in Europe is highly diverse in terms of clinical needs and processes. AD care practices in Finland, Germany, and Greece (the three national Alzheimer's organizations participating in 2D-BioPAD) differ based on their healthcare systems.

Diagnosing AD is complex, particularly in the early stages, with a high risk of misdiagnosis<sup>2</sup> and unnecessary treatments.<sup>3</sup> The cost of diagnostics, especially advanced tests like PET scans and MRIs, is prohibitive for many, posing a significant barrier.<sup>4</sup> Recent studies suggest that the use of plasma biomarkers (i.e., p-Tau217) could avoid approximately 57% of PET scans needed for selecting the appropriate treatment option, potentially reducing costs and improving accessibility.<sup>5</sup> The diagnostic process is also time-intensive, with long waits for diagnostic results and follow-ups. Clinical heterogeneity and lack of standardized practices further complicate diagnosis and research, as does the lack of digital interoperability, which hampers data sharing and collaboration. The aging population exacerbates these challenges,<sup>6</sup> increasing demand for dementia diagnostics and straining unprepared primary healthcare systems.<sup>7</sup>

Therefore, 2D-BioPAD refined a specific list of potential blood-based biomarkers as promising, convenient, cost-effective, and less invasive alternatives, following a clinical care pathway to address various needs, challenges, and barriers in AD management including

- Early detection of AD onset (e.g., SCI or MCI) at primary healthcare;
- Differential diagnosis and treatment selection at specialized care;
- Monitoring treatment response and disease progression at specialized care.

The 2D-BioPAD project aims to create a non-invasive, cost-effective tool for early AD diagnosis, with the goal of improving the treatment outcomes and reducing burdens. This project addresses the current challenges such as lengthy diagnostic timelines and inadequate biomarker diagnostics. In developing effective diagnostic tools for AD, it is crucial to differentiate between functional and non-functional technical specifications. Making this distinction ensures a comprehensive understanding of the system's requirements and supports the successful design and implementation of innovative diagnostic solutions.

\_

Boustani, M. et al., <u>Implementing a screening and diagnosis program for dementia in primary care</u> Journal of general internal medicine, 20(7), 572-577 (2005).

Howard, R., & Schott, J., When dementia is misdiagnosed International Journal of Geriatric Psychiatry, 36(6), 799-801 (2021).

Depends greatly on the equipment, e.g., 1T vs 3T MRI, etc.

Mattsson-Carlgren, N. et al., <u>Plasma biomarker strategy for selecting patients with Alzheimer disease for antiamyloid Immunotherapies</u>
JAMA neurology, 81(1), 69-78 (2024).

https://www.who.int/news-room/fact-sheets/detail/ageing-and-health

Kahn, S. D., & Terry, S. F. Who owns (or controls) health data? Scientific Data, 11(1), 156 (2024).

Teunissen, C. E. et al., <u>Blood-based biomarkers for Alzheimer's disease: towards clinical implementation</u> The Lancet Neurology, 21(1), 66-77 (2022).



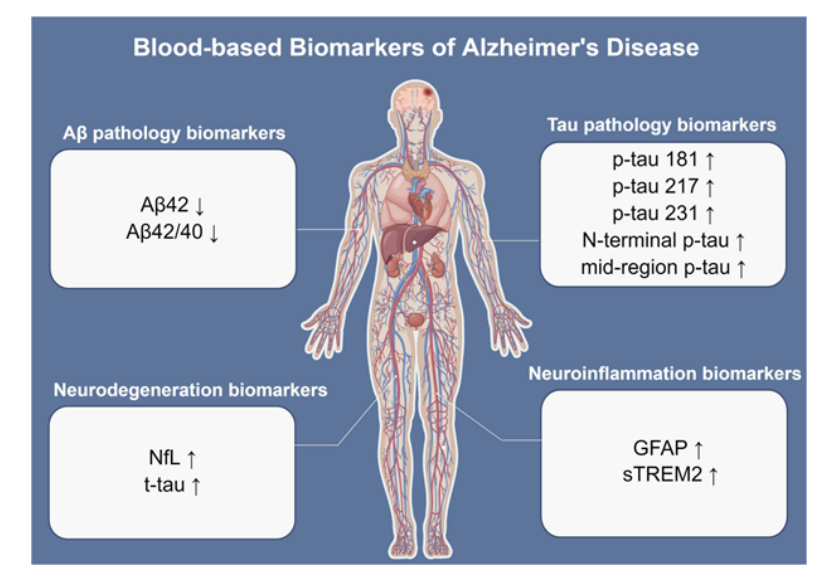


Figure 1: Overview of 2D-BioPAD AD biomarkers<sup>9</sup>.

These nanomaterials have been used to detect blood biomarkers like A $\beta$ 40, A $\beta$ 42, and p-Tau with good selectivity, specificity, fast response, and low limits of detection (LOD), across different stages of AD. <sup>10,11</sup>

Aptamers offer a validated alternative to antibodies for diagnostic and analytical applications, including the quantitative detection of Alzheimer biomarkers.<sup>12,13</sup> Compared to antibodies, aptamers provide a lower LOD, higher stability, lower cost and more flexible design while also being capable of distinguishing between different isoforms of the same protein.<sup>14,15</sup>

Identified using SELEX, aptamers face challenges like lengthy development times and low success rates, <sup>16,17</sup> but advancements in selection methods are improving outcomes. <sup>18,19</sup> with respect to traditional ELISA methods. <sup>20, 21, 22, 23</sup>. However, creating aptasensors that can simultaneously detect multiple biomarkers remains a challenge.

Tao, Q. Q., Lin, R. R., & Wu, Z. Y. <u>Early Diagnosis of Alzheimer's Disease: Moving Toward a Blood-Based Biomarkers Era</u> Clinical Interventions in Aging, 353-358 (2023).

Devi, R. et al., <u>Au/NiFe2O4 nanoparticle-decorated graphene oxide nanosheets for electrochemical immunosensing of amyloid beta peptide</u> Nanoscale Advances, 2(1), 239-248 (2020).

Chiu, M. J. et al., Nanoparticle-based immunomagnetic assay of plasma biomarkers for differentiating dementia and prodromal states of Alzheimer's disease—A cross-validation study Nanomedicine: Nanotechnology, Biology and Medicine, 28, 102182 (2020).

Scarano, S. et al. <u>Detecting Alzheimer's disease biomarkers: From antibodies to new bio-mimetic receptors and their application to established and emerging bioanalytical platforms e A critical review Analytica Chimica Acta 940 21e37 (2016).</u>

Zamanian,J. et al. <u>Current progress in aptamer-based sensing tools for ultra-low level monitoring of Alzheimer's disease biomarkers</u> Biosensors and Bioelectronics 197, 113789 (2022).

Mikuła E. Recent Advancements in Electrochemical Biosensors for Alzheimer's Disease Biomarkers Detection Current medicinal chemistry, 28(20), 4049–4073 (2021).

<sup>&</sup>lt;sup>15</sup> Zheng, Y., et al. <u>Advances in aptamers against Aβ and applications in Aβ detection and regulation for Alzheimer's disease</u> Theranostics, 12(5), 2095–2114 (2022).

Tuerk, C., & Gold, L. Systematic evolution of ligands by exponential enrichment: RNA ligands to bacteriophage T4 DNA polymerase Science, 249(4968), 505-510 (1990).

Ellington, A. D., & Szostak, J. W., In vitro selection of RNA molecules that bind specific ligands Nature, 346(6287), 818-822 (1990).

<sup>18</sup> Chen, Z. et al., Artificial intelligence in aptamer–target binding prediction International journal of molecular sciences, 22(7), 3605 (2021).

Mikuła, E., & Malecka-Baturo, K. <u>An Overview of the Latest Developments in the Electrochemical Aptasensing of Neurodegenerative Diseases</u> Coatings, 13(2), 235 (2023).

Khang, A. et al., A cost-effective aptasensor capable of early diagnosis and monitoring of Alzheimer's disease with the rapid analysis of beta-amyloid peptide 1–40 Sensors & Diagnostics, 2(2), 409-417 (2023).

Negahdary, M. et al., Aptasensing of beta-amyloid (Aβ (1– 42)) by a 3D-printed platform integrated with leaf-shaped gold nanodendrites Sensors and Actuators B: Chemical, 393, 134130 (2023).

<sup>&</sup>lt;sup>22</sup> Jia, Z. et al., <u>CRISPR-Powered Aptasensor for Diagnostics of Alzheimer's Disease</u> ACS sensors, 9(1), 398-405 (2023).

Phan, L. M. T., & Cho, S. <u>Fluorescent aptasensor and colorimetric aptablot for p-Tau231 detection: Toward early diagnosis of Alzheimer's disease</u> Biomedicines, 10(1), 93 (2022).



A list of 2D-BioPAD AD biomarkers under study is depicted in Figure 1 with relative descriptions reported below.

Beta amyloid (Aβ):	Under normal conditions, $A\beta$ is a soluble product of neuronal metabolism essential for synaptic function. A $\beta$ 40 and A $\beta$ 42 monomers are crucial for synaptic plasticity and neuronal survival. These plaques can disrupt neural networks and communication. When A $\beta$ 4 accumulates in the brain, its levels decrease in CSF and blood, and making A $\beta$ 4 a core biomarker for AD.
Tau protein (tau):	Tau protein, primarily associated with axonal microtubules, plays a role in signaling within dendrites. <sup>28</sup> Under pathological conditions, tau becomes hyperphosphorylated and forms neurofibrillary tangles (NFTs), leading to microtubule disintegration, disrupted signaling, and cell death. <sup>29</sup> Research and commercial assays focus on various phosphorylated forms of tau, including p-Tau181, p-Tau217, and p-Tau231, which are associated with different stages of AD progression.
Neurofilament Light and Neurodegeneration (NFL):	Neurofilament light (NFL) polypeptide, a component of the neural cytoskeleton, is a well-established marker of neuroaxonal injury and neurodegeneration. Under normal conditions, Plasma NFL correlates well with CSF measures for both MCl and AD, <sup>30</sup> making it a good blood-based biomarker. NFL is not specific to AD, as it also indicates other types of neurodegeneration, including different dementia types such as frontotemporal, vascular, and HIV-associated dementias. <sup>31</sup>
Glial fibrillary acidic protein (GFAP):	Glial fibrillary acidic protein (GFAP) is a well-studied glial marker released in response to A $\beta$ pathology. <sup>32</sup> GFAP, found in astrocytes, is released into CSF and blood when these cells are damaged.

Parihar, M. S. et al., <u>Amyloid-β as a modulator of synaptic plasticity</u> Journal of Alzheimer's Disease, 22(3), 741-763 (2010).

Hampel, H. et al., <u>The amyloid-β pathway in Alzheimer's disease</u> Molecular psychiatry, 26(10), 5481-5503 (2021).

<sup>26</sup> Klafki, H. W. et al., <u>Is plasma amyloid-β 1–42/1–40 a better biomarker for AD than AβX–42/X–40?</u> Fluids and Barriers of the CNS, 19(1), or (2022)

<sup>96 (2022).</sup>Pais, M. V. et al., Plasma biomarkers of Alzheimer's disease: a review of available assays, recent developments, and implications for

clinical practice Journal of Alzheimer's Disease Reports, (Preprint), 1-26 (2023).
 Grundke-Iqbal, I. et al., Abnormal phosphorylation of the microtubule-associated protein tau (tau) in Alzheimer cytoskeletal pathology

Proceedings of the National Academy of Sciences, 83(13), 4913-4917 (1986).
 Mietelska-Porowska, A. et al., <u>Tau protein modifications and interactions: their role in function and dysfunction</u> International journal of molecular sciences, 15(3), 4671-4713. (2014).

Gaetani, L. et al., <u>Neurofilament light chain as a biomarker in neurological disorders. Journal of Neurology</u>, Neurosurgery & Psychiatry, 90(8), 870-881 (2019).

Bridel, C. et al., <u>Diagnostic value of cerebrospinal fluid neurofilament light protein in neurology: a systematic review and meta-analysis</u>. JAMA neurology, 76(9), 1035-1048 (2019).

Morgan, A. R. et al., <u>Inflammatory biomarkers in Alzheimer's disease plasma</u>. Alzheimer's & dementia, 15(6), 776-787 (2019).



### WP2: Biomarkers Binding: Quantitative Analysis

WP2 named Biomarkers binding and quantitative analysis includes 4 tasks, and 4 deliverables outlined in Figure 2. Currently all Tasks of WP2 are underway.

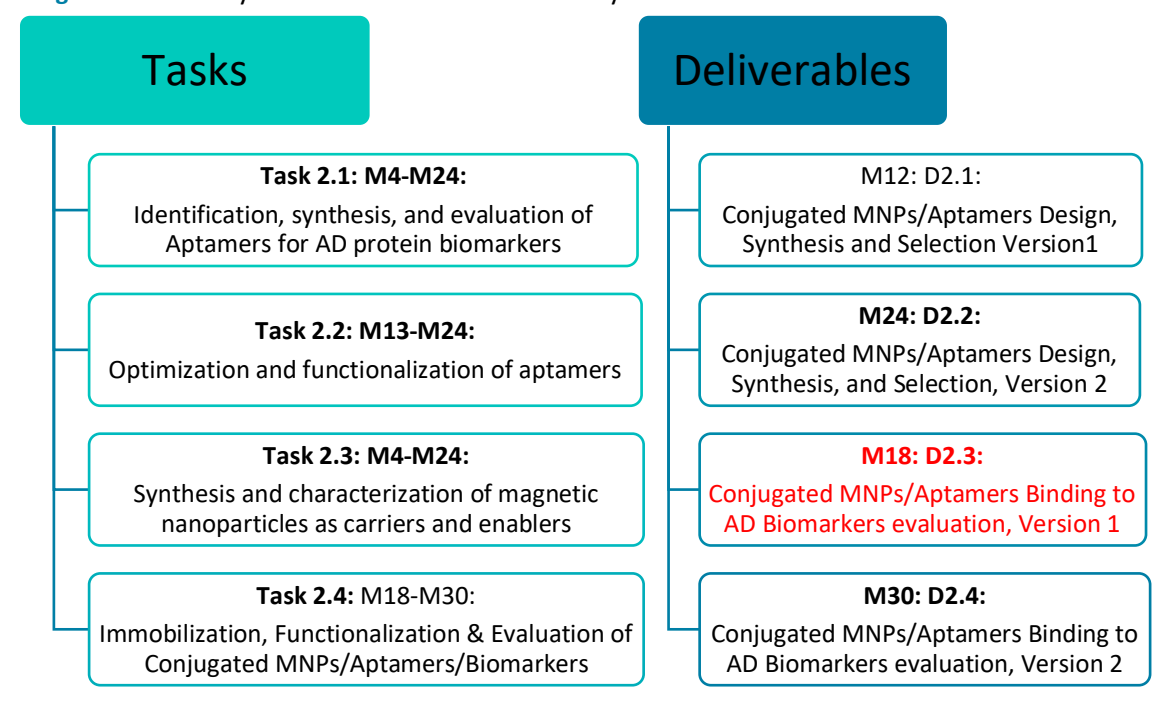


Figure 2: Schematic outline of Work Package 2: Biomarkers binding and quantitative analysis.

What follows is a brief progress report per task for WP2:

#### Task 2.1: Identification, Synthesis, and Evaluation of Aptamers for AD Protein Biomarkers

This task began with the identification of aptamers specific to AD protein biomarkers, such as Aβ 40, Aβ40, tau<sub>181</sub>, tau<sub>217</sub> tau<sub>231</sub>, NFL and GFAP. The process involved an extensive literature review and database search to collect all available DNA aptamer sequences that have been previously reported for these targets. Following this, a comparative study is underway to evaluate the characteristics, binding properties, and quantification techniques of the aptamers suggested. In cases of not effective literature aptamers, new aptamer selections are launched. Eventually, DNA aptamers, with the most robust properties, are evaluated for their binding affinity using techniques like Surface Plasmon Resonance (SPR) or BioLayer Interferometry (BLI) under appropriate buffer and reaction conditions. This exploration process is incrementally guided as the selected aptamers by deep learning models capable of predicting structures of high affinity, easing the process after each iteration. The evolution of the pools is monitored by NGS sequencing, and the sequence analyses which use a proprietary algorithm. Candidates chosen based on the bioinformatics analysis will be chemically synthesized and their binding to proteins will be characterized by SPR or BLI.

#### Task 2.2: Optimization and functionalization of aptamers

DNA aptamer length affects its immobilization and cost. Specifically, the longer the aptamer, the lower the immobilization effectiveness might be. In this task, the size optimization of aptamers is evaluated. Truncated variants of aptamers will be designed based on their predicted secondary structure,



chemically synthesized, and studied with respect to their binding properties (SPR or BLI). Aptamers corresponding to the minimal oligonucleotide displaying the properties of the parent aptamer are further elaborated while one of the 2 fixed flanks of the full-length aptamer may serve for immobilization purposes on MNPs evaluated by either SPR or BLI. These binding properties will be used as features to, along with the structure, train a deep learning model aiding length optimization.

#### Task 2.3: Synthesis and Characterization of Magnetic Nanoparticles as Carriers and Enablers

This task focuses on the synthesis and characterization of MNPs to be utilized as carriers and enablers in bioassays, facilitating sample purification, minimizing non-specific signals, and controlling flow during various stages, such as bioreceptor incubation, purification, recognition, and signal acquisition. Magnetite ( $Fe_3O_4$ ) MNPs have been synthesized with a focus on producing nanoparticles of varying sizes and are currently rigorously characterized structurally, morphologically, and magnetically (TEM, XRD, VSM) since the size of the MNPs is directly reflected to their magnetic response and in turn their interaction with external magnetic fields while may affect specifically and selectively the aptamer immobilization to be held in T2.4. To provide electrochemical sensing via electrical conductivity biphasic MNPs, a gold shell surrounds the magnetic core in a  $\sim$  50 nm diameter core-shell formulation. These MNPs are critical for facilitating sample purification, reducing non-specific signals, and controlling the flow of materials at various stages of the bioassay, where required. The integration of MNPs ensures that the aptamers remain oriented and functional throughout the bioassay process, enhancing the overall reliability and accuracy of biomarker detection.

# Task 2.4: Immobilization | Functionalization | Evaluation of Conjugated MNPs / Aptamers / Biomarkers

Well established cross-linking methodologies for DNA sequences immobilization on MNPs are currently examined and evaluated. Following, a systematic investigation of the binding capacity of conjugated MNPs/Aptamers with the selected biomarkers is underway.

WP2 Biomarkers binding and quantitative analysis initiated with an extended literature review and search in databases for all the available sequences of DNA aptamers for the selected biomarkers, towards selecting the most appropriate primary structure, and designing the secondary structure according to the sensing strategies.

Currently, the required aptamers are selected and already conjugated effectively with MNPs for thrombin (reference case), Aβ40 and Aβ40 aptamers with respect to individual aptamer design optimization (size, buffer, ionic strength, pH, etc.), GFAP conjugation process and efficiency testing is underway, while for NFL and Tau (tau<sub>181</sub>, tau<sub>217</sub> tau<sub>231</sub>) aptamer optimization and selection process is expected in the upcoming months by NovapTech SELEX procedure, employing proprietary random oligonucleotide libraries and AI techniques (CeADAR) with emphasis on selectivity and sensitivity.

The conjugated MPNs/Aptamers are tested at lab environment with all biomarkers to evaluate their binding capacity. Finally, possible redesign and optimization might be needed after the first testing. Immobilization on MNPs might change the binding capacity and specificity of the aptamers. Thus, it is essential to validate MNPs/aptamers performance at the different stages of the final sensor manufacture to ensure results' reliability and reproducibility.



## 2. Aptamers' Identification

Novaptech focuses on the identification of aptamers and evaluation of their binding affinity to AD protein biomarkers. Before starting the aptamer selection process (SELEX), Novaptech has performed literature search to find the already reported aptamers against Aß40 and Aß42 peptides, tau proteins phosphorylated at specific sites, GFAP and NFL. As discussed in deliverable D2.1, the binding of the literature aptamer to Aß40 and Aß42 peptides could not be verified. The literature aptamers are not available for other biomarkers. Next, the aptamer selection process (SELEX) was carried out against different biomarkers. The selections were followed by characterization of selected aptamers by standard techniques of biomolecular interaction such as surface plasmon resonance (SPR), bio-layer interferometry (BLI), etc. Well characterized aptamers thus obtained will be used as a recognition element in the different sensors systems being developed by other partners of the consortium. The aptamers offer added advantages in comparison to traditional antibodies, because aptamers can provide increased flexibility in terms of handling & modification thus enhancing integration capability in sensors. Below is the summary/overview of aptamer selection process for all the biomarkers:

Aß40 and Aß42 peptides: These peptides pose considerable challenges when subjected to ssDNA pooltarget incubation steps during the aptamer selection process. This is a critical step where a peptide structure plays the utmost important role in recognizing the cognate aptamer candidates. Our last aptamer selection against both peptides failed to show any enrichment and did not yield aptamers. The most probable reasons for not getting enrichment could be unstable structure due to aggregation propensity of these peptides. Aptamer selection depends entirely on the target structure/form and hence the target must maintain the identical structure/form throughout the selection. The aggregation propensity of these peptides is a deterrent in the evolution of aptamer pools. Hence, after several attempts of aptamer selection, we requested assistance from SIAB members and potential experts outside the consortium. (Prof. Y. Sarigiannis, Department of Health Sciences, School of Life & Health Sciences, University of Nicosia, Dr. Hans Michael Maric, Emmy Noether Group Leader Chemical Biology, Rudolf Virchow Center - Center for Integrative and Translational Bioimaging, University of Würzburg, Dr. Hans Klafki, Dept. of Psychiatry and Psychotherapy, University Medical Center Goettingen, Dr. Hermann Esselmann, Leitung Forschungskoordination, Universaetsmedizin Goettingen). We conducted several extra dedicated on-line meetings with the experts on issues raised during aptamer selection process and we are currently examining alternative AB peptides following modified handling protocols and evaluate pre-treated peptides in the desired form<sup>33</sup>.

**GFAP:** As there were no literature aptamers for GFAP, multiple new aptamer selections were launched against GFAP. From one of the selections, we found multiple candidates which could recognize GFAP and these results were already shared in the last deliverable. Some new developments on the same aptamers are given here and few of these aptamers were subjected to kinetics studies (testing against a series of GFAP conc.).

Single cycle kinetic analysis was performed with several identified aptamers, namely FIB001A, FIB007A, FIB002B, FIB012B, FIB001C and FIB011C. To determine the binding constants, aptamers were captured on the CM5 SPR chip via hybridization to an anchor oligo and GFAP protein of conc. 25, 50, 100, 200 and 400 nM was flown over the chip. In another experiment, aptamers FIB007A and FIB002B were subjected to kinetics in the GFAP conc. of 11, 22, 45, 90 and 180 nM using the same

<sup>33</sup> See Appendix I



methodology. Although the accurate kinetic parameters couldn't be extracted because the complex didn't dissociate during the time of the analysis, it can be observed that the aptamer/GFAP complexes are characterized by a  $K_D$  value in the low nanomolar range (see Figure 3).

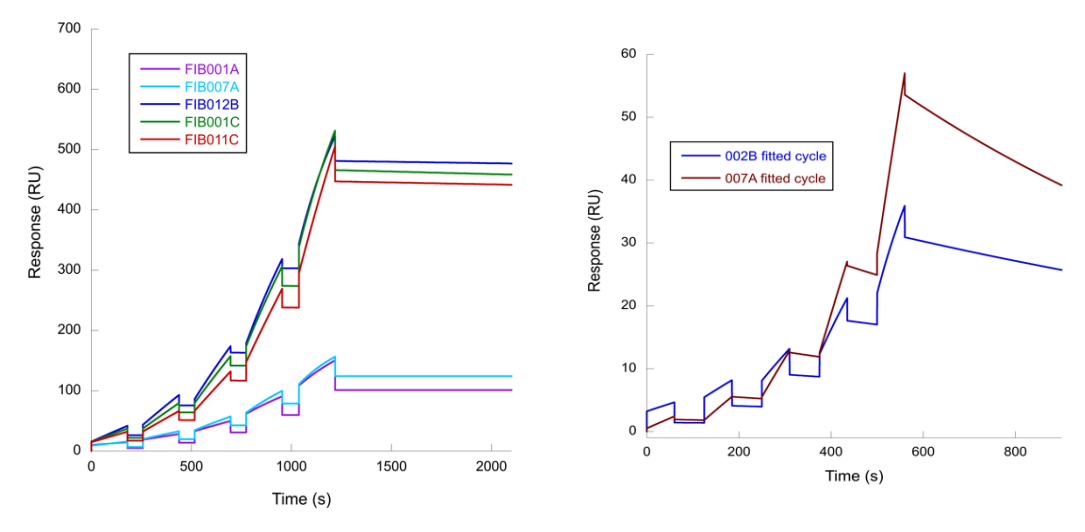


Figure 3: Single cycle kinetics analysis of the binding of aptamers to GFAP; left- 25, 50, 100, 200 and 400 nM GFAP conc., and right- GFAP conc. of 11, 22, 45, 90 and 180 nM

Besides this, there are other ongoing selections for GFAP, and to find the best candidates, many selection parameters, such as a) different proprietary libraries, b) stringency conditions, c) buffers, d) competitive strategies, etc. were varied in these selections. We monitor the progress during the selection by maintaining the quality and quantity of ssDNA pools obtained after each selection round. The pools are sequenced after SELEX and bioinformatics analyses (Next Generation Sequencing analysis) are carried out on these pools. For many analyzed pools, NGS showed good enrichment in these selections. The successful enrichment of some projects for GFAP is shown in Figure 4.

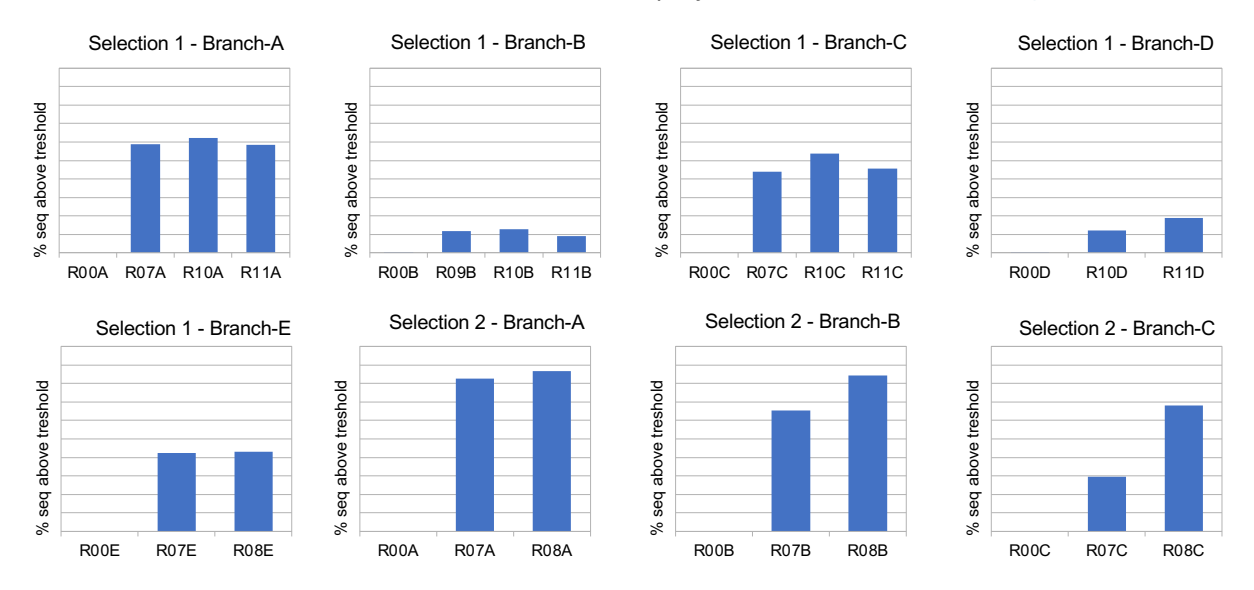


Figure 4: Evolution of pools highlighted by enrichment in two GFAP selections. The height of the bars represents the percentage evolution achieved during selections at different rounds.

The motif prediction analysis of these evolved pools indicated that identification of multiple motifs (the motifs signatures are not given in this report for data confidentiality). To describe, the identified motifs are shown in the form of motif logos, where the motifs are the conserved sequences found in



multiple sequences in the pools. The higher frequency of a motif combined with a strong conservation in motif logo can indicate the association of the motif sequence with the target. Although it's a must to add that these all are predictions and a validation of the same requires biophysical characterization and binding affinity analyses.

Further, the evolutionary profile was also studied by clusterization and secondary structure prediction. For some candidates, the G-rich regions could not give secondary structure elements and hence to better know the G4 making potential of these candidates and logos, some circular dichroism (CD) spectra can be obtained, which will be a next step, if more information about the specific structure is needed. However, despite these limitations, the motifs identified were mapped to the secondary structures to identify the key secondary structure elements such as bulges, loops, stems, etc. to gain a broader picture of possible candidates which could bind GFAP. Few representative secondary structures (not actual) along with motifs (representative) have been highlighted in Figure 5.

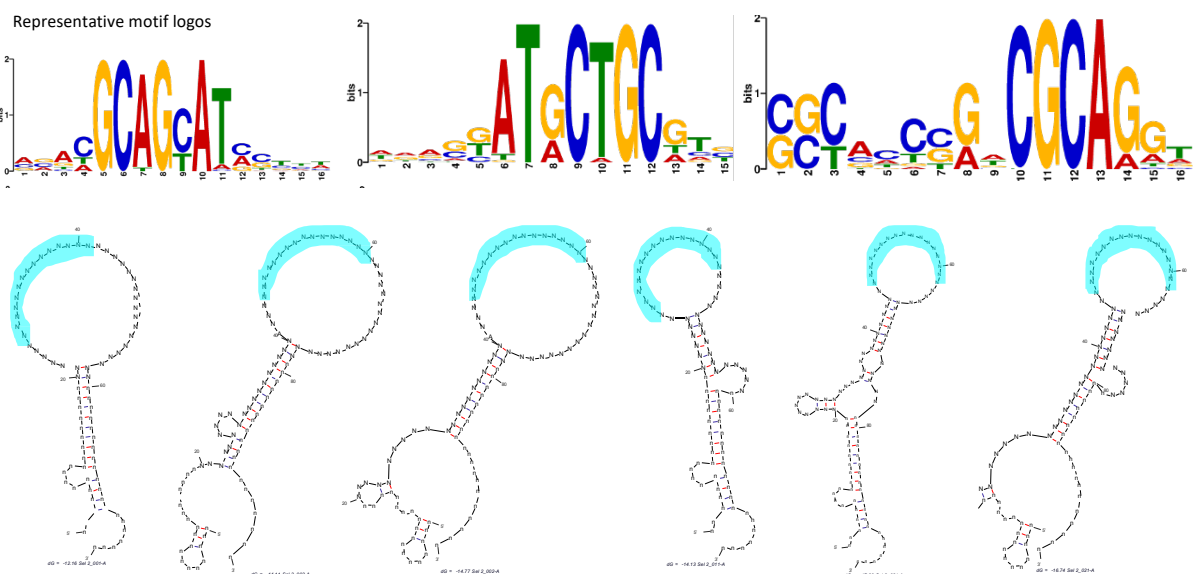


Figure 5: Representative motif logos generated by motif analysis. At the bottom, A motif logo has been mapped to the secondary structures. All the sequences and logos shown are for representation of the process, while actual sequences and logos have been not shown.

On the basis of presence of motifs, clustering and secondary structures, the representative sequences were selected for further biophysical characterization. The binding properties of these candidates will be studied via SPR or BLI.

It is worth mentioning that some GFAP aptamers are already identified from a previous GFAP selection project which was also shared in the last deliverable. Currently, the candidates for this selection have been length-optimized and have been discussed under section 3. Aptamers' Optimization.

**NFL:** Similar to the GFAP biomarker, multiple new aptamer selections were also launched against NFL biomarker. To find the best candidates, many selection parameters, such as a) different proprietary libraries, b) stringency conditions, c) buffers, d) competitive strategies, etc. were varied in these selections. During the selection, the process was monitored by maintaining the quality and quantity of ssDNA pools obtained after each selection round.



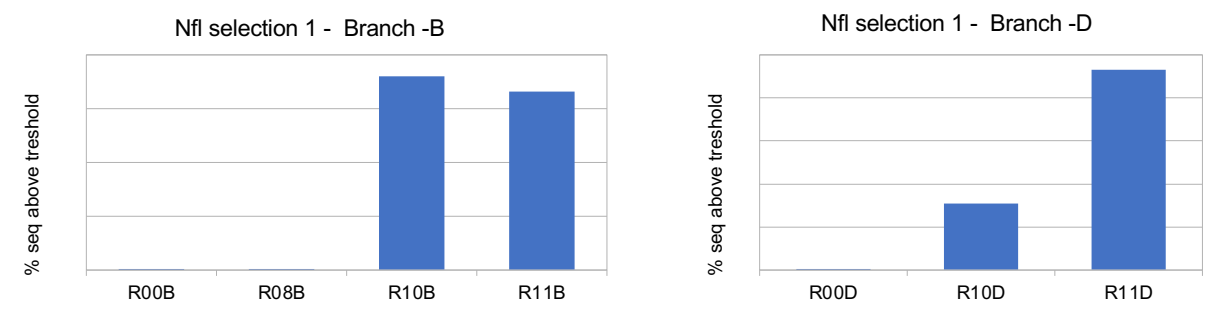


Figure 6: Evolution of pools highlighted by enrichment in a Nfl selection. The height of the bars represents the percentage evolution achieved during selections at different rounds.

The pools were sequenced after SELEX and bioinformatics analyses (Next Generation Sequencing analysis) were carried out on these pools. NGS showed good enrichment in these selections. The successful enrichment of some NFL aptamer selection projects at different rounds during the selection has been shown in Figure 6. As a representative image, Figure 7 below shows the secondary structures predicted for a few candidates from NFL pools.

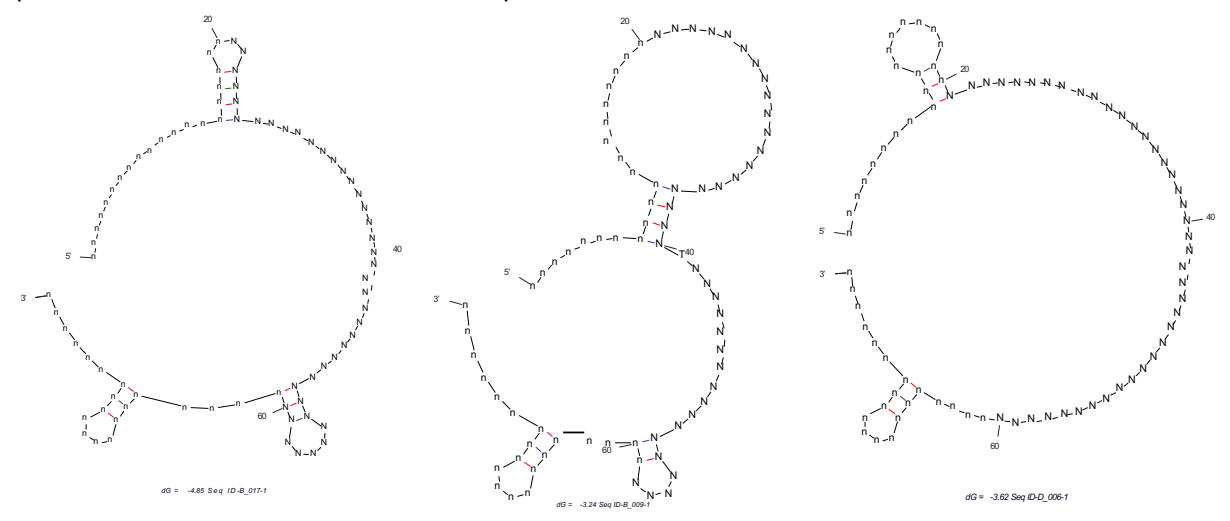


Figure 7: Secondary structure prediction of few candidates from Nfl pools. Here, the sequences have been coded (sensitive data).

From a particular selection, the following representative candidates (**Table 1**) were selected for further biophysical characterization where the decision to choose a particular candidate was made on the presence of relative frequencies, motif sequences, clustering and secondary structures.

Table 1: Selected candidates from NFL pools for biophysical characterization.

Name	Length (nt)
AFA002D2	81
AFA005B	80
AFA023B	80

We proceeded with the evaluation of all the candidates listed in **Table 1** by SPR. To this end these oligonucleotides were immobilized on the streptavidin sensor chip by hybridization to a



complementary biotinylated capture oligonucleotide. Then an NFL solution was injected over the chip at different concentrations in the selection buffer. In a second step the buffer only was injected. The starting libraries were used as a negative control. The resonance signal was recorded during the association and dissociation phases.

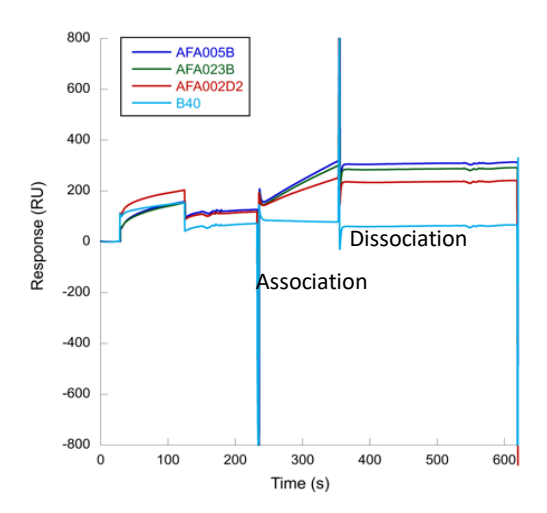


Figure 8: Sensor grams obtained for the interaction between the different oligonucleotide candidates and NFL (80 nM). The library (B40) used for the selection were used as references.

The sensograms obtained at 80 nM NFL are shown in Figure 8. All three candidates generated a strong resonance signal characterized by a very fast association and a slow dissociation. Due to extremely stable complexes, the dissociation did not take place and hence determination of  $K_D$  was not possible here. Although as per the strong responses and conc. tested it should be in the low nanomolar range for these candidates. In conclusion we obtained strong aptamers for NFL.

For specificity studies, all three NFL aptamers were also tested at 80 nM of GFAP protein. At this concentration, NFL aptamers also recognized GFAP which can be seen in **Figure 9**. Hence these candidates also require more specificity studies. To enhance the specificity, some NFL specific motifs can be targeted for truncations. These aptamers will be further truncated in effort to enhance the specificity of aptamers towards NFL.

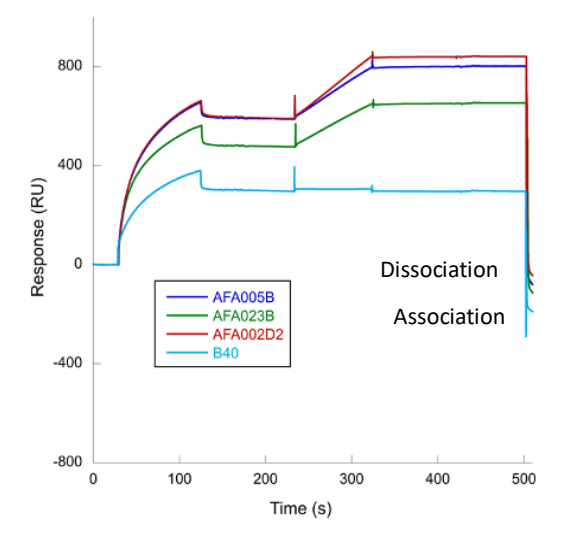


Figure 9: Sensorgrams showing interaction of GFAP with NFL candidates at 80 nM concentration.

The library (B40) used for the selection was used a reference.



Besides this, multiple other selections are currently under progress and stand at different stages such as selection, bioinformatics analysis or characterization. The selections where bioinformatics analysis has been performed show good enrichment (see Figure 10). These selections have used various selection strategies (as for GFAP biomarker) to yield high quality aptamers.

For these selections, the bioinformatics analysis showed promising sequences enrichments, motifs and secondary structure predictions. Some representative secondary structures highlighting identified motifs from these selections are shown in Figure 11. The representative sequences from these pools will be synthesized and characterized for their binding with NFL protein.

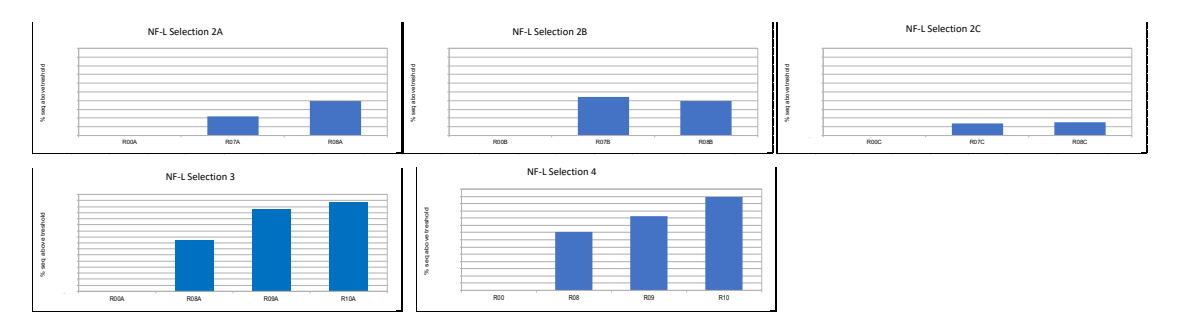


Figure 10: Evolution of pools highlighted by enrichment in multiple NFL aptamer selection projects. The height of the bars represents the percentage evolution achieved during selections at different rounds.

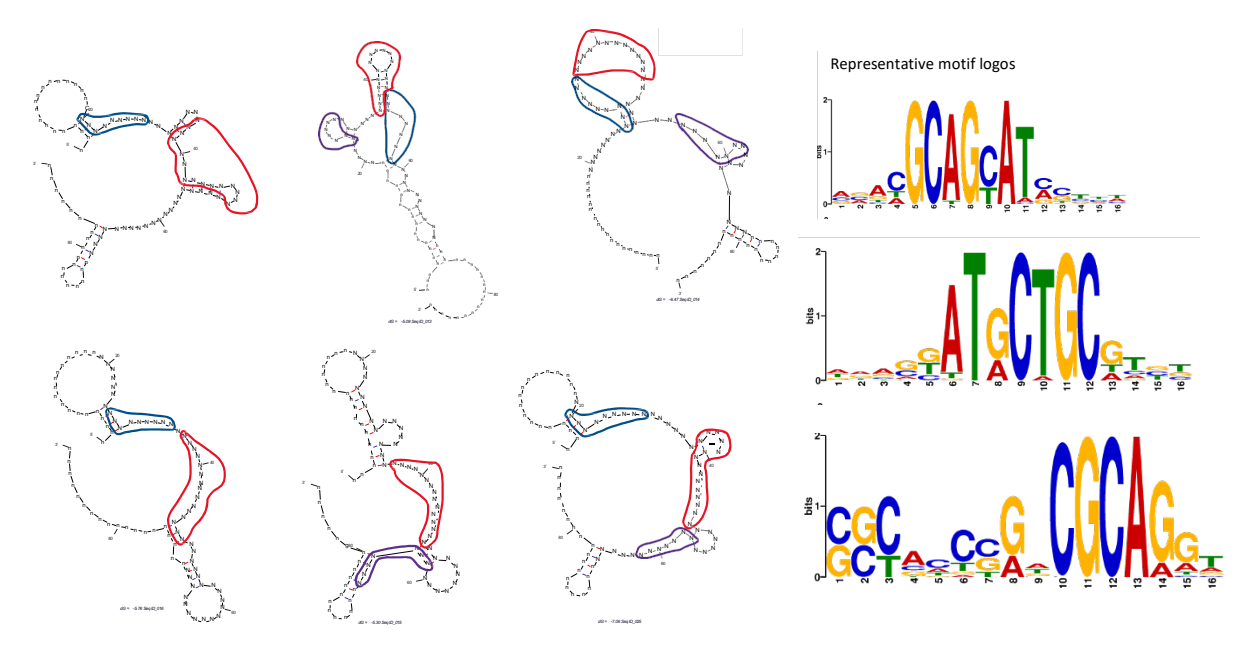


Figure 11: The motifs identified for the NFL selections are highlighted in the coded secondary structures. On right, representative motif logos are shown.

pTau-217 protein: The aptamer selection against this protein was challenged with the unavailability of the target. To specifically target pTau-217, the protein used for selection must not contain other phosphorylated sites. Since tau protein is prone to phosphorylation, it will also have multiples other phosphorylated residues, hence using the full-length protein as target was not possible here. After several discussions with commercial suppliers and collaborators, it was decided to work with the peptide sequence containing the region of interest which will be phosphorylated at the desired



residue. To this end, a peptide sequence covering the region of interest was synthesized with phosphorylation at the desired threonine amino acid. The peptide sequence is SRTPSLP-Tphos-PPTREPKKVA, where Tphos is phosphorylated threonine. This peptide sequence represents the epitome of the interest in this protein. For a negative selection strategy, where a negative selection will discard the sequences showing affinity to the non-phosphorylated peptide, we also synthesized a non-phosphorylated peptide. The sequence of this peptide was same, except the phosphorylation at the threonine residue.

The aptamer selection against these peptides is currently underway. To achieve this, an aptamer library with a random window of 40 nt, is being utilized. As described above, the selection strategy also uses a negative selection round, which enhances the probability of picking candidates against phosphorylated form only. The enrichment and NGS data for this selection is likely to be available by end of April, 2025.

As a part of this effort, CeADAR conducted a literature search to identify, compare, and assess advanced computational methodologies used in aptamer binding research. These methodologies span a broad spectrum of techniques, from experimental approaches enhanced by machine learning to state-of-the-art transformer-based models designed for predicting and generating high-affinity aptamer sequences. Each method was meticulously evaluated based on its core description, key features, and inherent limitations, which subsequently informed their functionality ratings and suitability for specific research contexts.

Namely, MLPD<sup>34</sup>, RaptGen<sup>35</sup>, AptaNet<sup>36</sup>, APIPred<sup>37</sup>, AptaBERT<sup>38</sup>, AptaTrans<sup>39</sup>, and Apta-MCTS (Monte-Carlo Tree Search)<sup>40</sup> are included as outlined in Deliverable **D2.1**<sup>41</sup>.

#### Benchmarking Strategies for the Prediction of Aptamer-Target Binding:

#### Apta-MCTS (Machine Learning) and Apta-Trans (Deep Learning)

To optimize the discovery of high-affinity aptamer sequences, we employed two computational strategies as benchmarks:

- 1. Apta-MCTS (Machine Learning-based Approach, Figure 12)<sup>39</sup>
- 2. AptaTrans (Deep Learning-based Approach, Figure 13)<sup>38</sup>

Both models were designed to systematically generate and evaluate candidate aptamer sequences for targeted interactions, leveraging distinct algorithmic methodologies. The process was structured in two stages: (i) candidate sequence generation—using Monte Carlo Tree Search (MCTS) with a Random Forest (RF) classifier in Apta-MCTS (Figure 12) and a Transformer-based deep learning model in AptaTrans (Figure 13)—and (ii) computational binding affinity calculation, where selected

Bashir, A. et al., <u>Machine learning guided aptamer refinement and discovery</u> Nat Commun 12, 2366 (2021).

lwano, N. et al., <u>Generative aptamer discovery using RaptGen</u> Nat Comput Sci 2, 378–386 (2022).

Emami, N. et al., AptaNet as a deep learning approach for aptamer—protein interaction prediction Sci Rep 11, 6074 (2021).

<sup>&</sup>lt;sup>37</sup> Fang, Z. et al., APIPred: An XGBoost-Based method for predicting aptamer—protein interactions J. Chem. Inf. Model. 64, 7 (2023).

Morsch, F. et al., <u>AptaBERT: Predicting aptamer binding interactions bioRxiv</u>, 2023-11 (2023).

<sup>39</sup> Shin, I. et al., AptaTrans: a deep neural network for predicting aptamer-protein interaction using pretrained encoders BMC Bioinformatics 24, 447 (2023).

Lee, G. et al. <u>Predicting aptamer sequences that interact with target proteins using an aptamer-protein interaction classifier and a Monte Carlo tree search approach</u>. *PLOS ONE*, 16(6), e0253760 (2021).

<sup>&</sup>lt;sup>41</sup> D2.1 submitted on 30/09/2024.



sequences were structurally modelled using RNA Composer and calculated for binding potential via ZDOCK docking simulations (Figures 12 and 13).

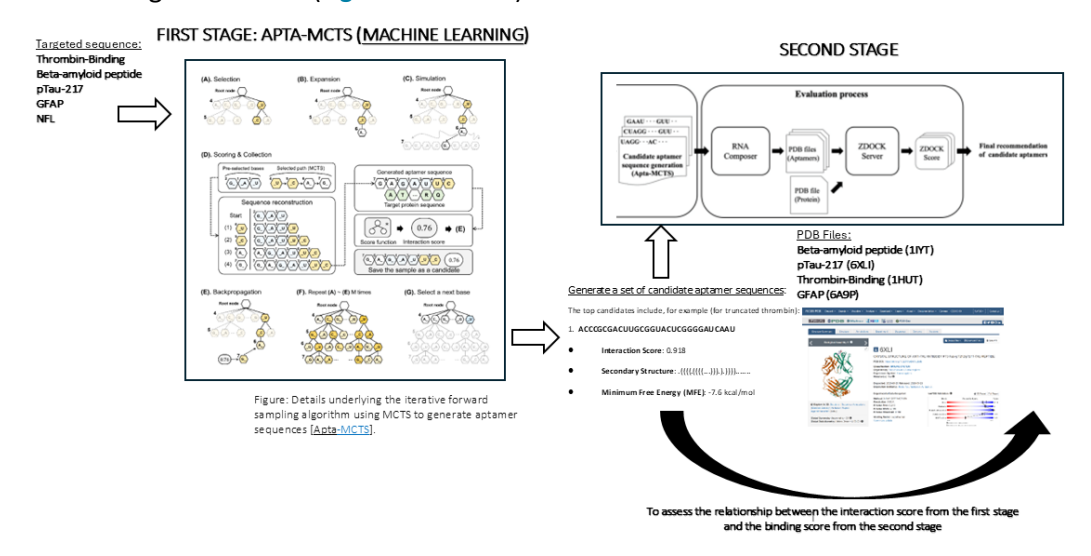


Figure 12: The Apta-MCTS pipeline for aptamer discovery, integrating Monte Carlo Tree Search (MCTS) with a Random Forest (RF) classifier trained on Li et al. (2014) and Lee and Han (2019) datasets. The process involves candidate aptamer generation, interaction score prediction, structural modeling with RNA Composer, and binding affinity calculation using ZDOCK, ultimately selecting high-affinity aptamers.

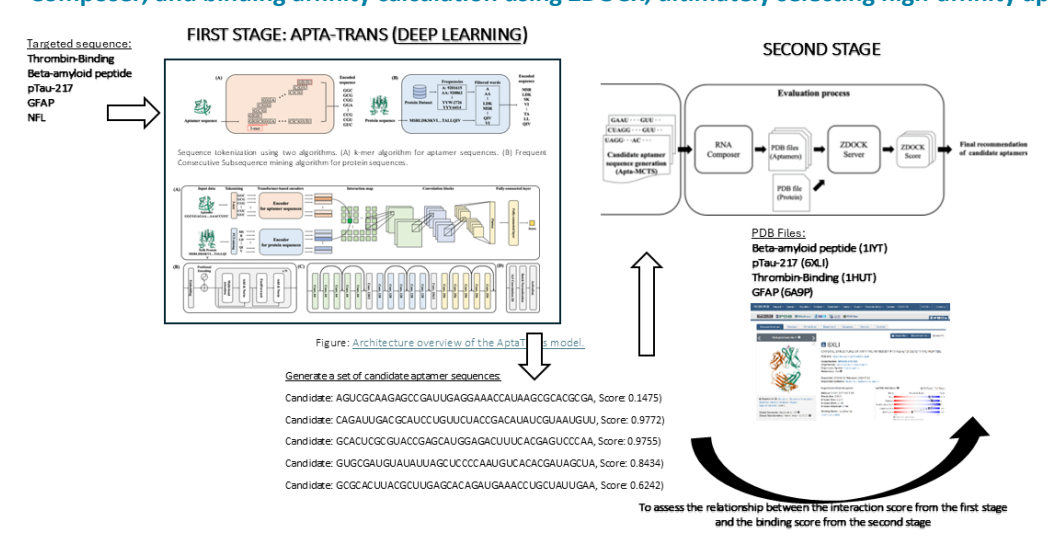


Figure 13: The AptaTrans pipeline, leveraging a Transformer-based deep learning model. It employs sequence tokenization and attention mechanisms for candidate aptamer generation, followed by structural modeling with RNA Composer and binding affinity calculation using ZDOCK, identifying the most promising aptamers.

#### Stage 1: Generation and Recommendation of Candidate Aptamer Sequences

#### Benchmark 1: Apta-MCTS (Machine Learning)

We employed a computational approach using the Apta-MCTS model, coupled with a RF classifier optimized for aptamer-protein interactions (API) prediction.<sup>39</sup> The process utilized a pre-trained RF



classifier applied to API data, derived from the benchmark dataset provided by Li et al. (2014)<sup>42</sup> and Lee and Han (2019)<sup>43</sup> (as detailed in **Table 2**). During the selection step (**Figure 14**), a path from the root to a leaf was determined using Upper Confidence Bounds applied to Trees (UCT) scores, calculated using a specified formula.

#### Initialization:

- The target protein sequence, such as the thrombin binding aptamer, and the desired length of the aptamer candidates are provided as inputs.
- The MCTS algorithm is initiated to explore the nucleotide sequence space, where each node represents a nucleotide base and complete paths from the root to the leaves correspond to full aptamer sequences.

#### **Sequence Sampling via MCTS:**

- The algorithm constructs sequences iteratively by selecting the most promising paths based on the UCT score. This scoring mechanism strikes a balance between exploration.
- For each generated sequence, the Apta-MCTS model employs the pre-trained RF classifier to evaluate the interaction potential between the aptamer and the target protein.

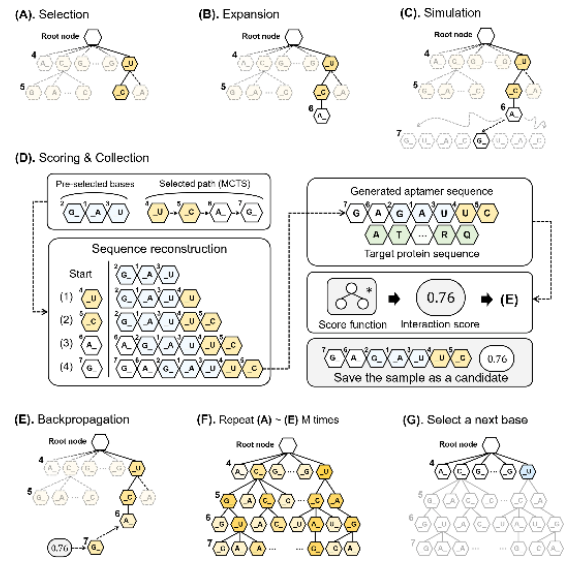


Figure 14: An iterative forward sampling algorithm, guided by Monte Carlo Tree Search (MCTS), was employed to generate aptamer sequences in a systematic manner.<sup>39</sup>

Table 2: Performance pre-trained RF classifier references.

Training set	Sensitivity	Specificity	Accuracy	Yuden's Index	МСС
Li et al. 2014 <sup>40</sup> (with 35, 39, 55 and 77 Trees)	0.290	1.000	0.822	0.290	0.484

<sup>&</sup>lt;sup>42</sup> Li, B. Q., Zhang, Y. C., Huang, G. H., Cui, W. R., Zhang, N., & Cai, Y. D. (2014). <u>Prediction of aptamer-target interacting pairs with pseudo-amino acid composition</u>. *PLOS ONE*, **9**(1), e86729.

<sup>&</sup>lt;sup>43</sup> Lee, W., & Han, K. <u>Constructive prediction of potential RNA aptamers for a protein target</u>. *IEEE/ACM Transactions on Computational Biology and Bioinformatics*, **17**(5), 1476-1482 (2019).



Training set	Sensitivity	Specificity	Accuracy	Yuden's Index	МСС
Lee and Han 2019 <sup>41</sup> (with 49 and 173 Trees)	0.982	0.571	0.777	0.554	0.607

#### **Iteration and Optimization:**

- MCTS refines its search by iterating over potential sequences, optimizing the selection process to maximize interaction scores predicted by the RF model.
- High-scoring sequence fragments are retained during each iteration, progressively narrowing the search space and reducing computational overhead.

#### **Post-Processing:**

- A large pool of candidate sequences is analyzed using the ViennaRNA package to predict their secondary structures. This step filters out redundant sequences with identical secondary structures, ensuring only unique and viable candidates are retained.
- The final list of aptamer sequences is ranked by their interaction scores, providing an optimized selection for experimental validation.

The classifier's performance was assessed using multiple evaluation metrics: sensitivity (Sn), specificity (Sp), accuracy (Acc), Youden's index (J), and the Matthews Correlation Coefficient (MCC). These metrics are expressed in terms of true positives (TP), true negatives (TN), false positives (FP), and false negatives (FN), where TP and TN represent correct predictions of APIs, and FP and FN represent incorrect predictions.

$$UTC_{i,s_{i},n_{i},N_{i}} \stackrel{\text{def}}{=} \frac{s_{i}}{n_{i}} + C \times \sqrt{\frac{ln(N_{i})}{n_{i}}}$$

$$Sn = TP/(TP + FN)$$

$$Sp = TN/(FP + TN)$$

$$Acc = (TP + TN)/(TN + FP + FN + TP)$$

$$J = Sn + Sp - 1$$

The MCC was calculated using the following formula:

$$MCC = \frac{(\mathit{TP}*\mathit{TN} - \mathit{FP}*\mathit{FN})}{\sqrt{(\mathit{TP} + \mathit{FP})(\mathit{TP} + \mathit{FN})(\mathit{TN} + \mathit{FP})(\mathit{TN} + \mathit{FN})}}$$

#### Benchmark 2: AptaTrans (Deep Learning)

We employed a deep learning-based approach using the AptaTrans model, leveraging transformer-based encoders optimized for API prediction.<sup>38</sup> The AptaTrans framework integrates self-supervised pretrained encoders that represent aptamer and protein sequences at the monomer level, addressing the structural and physicochemical complexities of API prediction. The model was trained and validated on benchmark datasets, including those derived from experimental aptamer-protein complex data.

#### Initialization:

The target protein sequence and candidate aptamer sequences were provided as inputs.



- AptaTrans encoders were pretrained using a masked token prediction (MTP) strategy and secondary structure prediction (SSP) to enhance sequence representation.
- The dataset was preprocessed by converting DNA aptamer sequences into RNA format and applying k-mer tokenization for aptamers and Frequent Consecutive Subsequence (FCS) mining for proteins.

#### **Sequence Processing via Transformer-Based Encoding:**

- AptaTrans employs transformer encoders to generate contextual embeddings for both aptamer and protein sequences.
- Interaction matrices were constructed by computing the dot product of token embeddings, capturing monomer-level sequence relationships.
- Convolutional layers extracted hierarchical features from the interaction matrices to predict API scores with high sensitivity and specificity.

#### **Iteration and Optimization:**

- The model was trained using a dataset consisting of 580 positive and 1,740 negative API pairs, with an additional 145 positive and 435 negative pairs for evaluation. A comprehensive distribution of both protein and RNA secondary structures is presented in Table 3.
- The encoder architecture included multi-head self-attention layers, feedforward networks, and GELU activation functions, optimized through the AdamW optimizer.
- Data augmentation was applied to generate symmetrical aptamer sequences, effectively doubling the training dataset.

Table 3: Distribution of protein and RNA secondary structures for pretraining.<sup>38</sup>

Types	PDB <sup>44</sup>	Types	bpRNA <sup>45</sup>
α-helix	32.74%	Stem	48.50%
eta-sheet	21.11%	Hairpin loop	22.51%
Turn	11.06%	Multi-loop	4.86%
eta-bridge	1.22%	Internal loop	7.51%
3 <sub>10</sub> helix	3.63%	Bulge	1.95%
Bend	9.15%	External loop	11.34%
Coil	20.45%	Psedoknot	3.33%
$\pi$ -helix	0.64%		

#### **Post-Processing:**

<sup>44</sup> Berman HM, Westbrook J, Feng Z, Gilliland G, Bhat TN, Weissig H, et al. The protein data bank. Nucleic Acids Res. 28(1), 235–42 (2000).

<sup>&</sup>lt;sup>45</sup> Danaee P, Rouches M, Wiley M, Deng D, Huang L, Hendrix D. bpRNA: large-scale automated annotation and analysis of RNA secondary structure. Nucleic Acids Res. 46(11), 5381-94 (2018).



• The final list of aptamer sequences is ranked by their interaction scores, providing an optimized selection for experimental validation.

For the binary classification task, we used six commonly used performance metrics: These performance metrics include the ACC, MCC, Sn, Sp (provided the formulas in the above section), ROC-AUC, and F1-score (F1), which are defined as follows:

$$ext{ROC}$$
 -  $ext{AUC} = \int_0^1 ext{ROC}(x) dx$   $ext{F1} = 2 imes rac{ ext{TP}}{ ext{TP} + ext{FP} + ext{FN}}$ 

where TP, TN, FP, and FN denote the true positives, true negatives, false positives, and false negatives, respectively. The ROC curve illustrates how the binary classification performance varies according to its discrimination threshold. ROC(x) represents the true positive rate, also known as the sensitivity, plotted against the false positive rate (1-specificity), for a given threshold x. The ROC-AUC is a crucial metric, particularly for the prediction of aptamer-protein Interaction. Predicting the interaction results in a binary outcome. An ideal model should have a high Sn and Sp, resulting in a high ROC-AUC value.

#### Stage 2: Structural Evaluation and Binding Affinity Calculation

Following the first-stage selection of aptamer candidates, the second stage focused on binding-affinity simulations to evaluate their structural compatibility with target proteins (see Figure 15).<sup>38</sup>

- 1. RNA Composer was employed to convert generated aptamer sequences into 3D structures for binding studies.
- 2. ZDOCK Server was used for protein-aptamer docking simulations, predicting interaction stability and binding scores. ZDOCK Score provides a measure of the structural compatibility between an aptamer and its target protein.

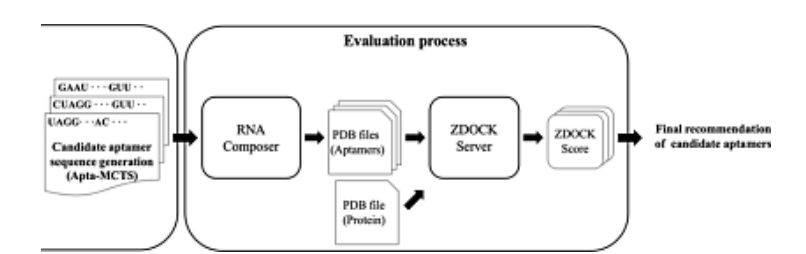


Figure 15: Candidate aptamer generation process and its analysis using the AptaTrans pipeline (including Apta-MCTS), RNA Composer, and ZDOCK Server.<sup>38</sup>

The entire workflow enabled that only high-affinity aptamer sequences with favorable binding scores will be shortlisted for further experimental validation.

#### **Results**

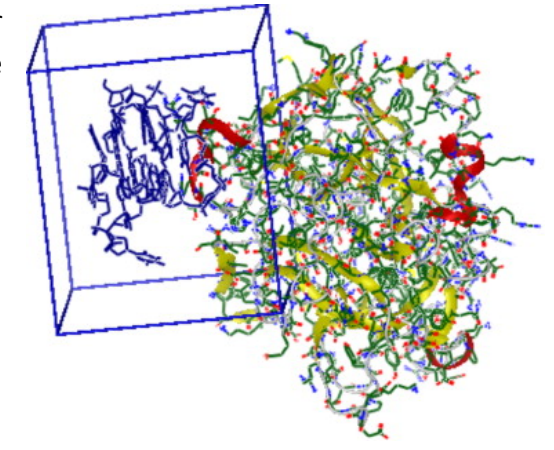
Structure-Guided Aptamer Selection for Thrombin Binding



The structure of the aptamer—thrombin complex, specifically the structure (Protein Data Bank (PDB) code: 1HAO), was retrieved from the PDB. This structure features the 15-mer thrombin-binding aptamer (TBA) in its characteristic chair conformation, which interacts with thrombin's fibrinogen-

binding exosite. The 15-mer TBA in its chair conformation served as the reference ligand for the simulation process (Figure 16).

Figure 16: A binding box around the fibrinogen-binding exosite of thrombin to encompass the 15-mer TBA, highlighted in blue. The thrombin structure, including its secondary structure details, was retrieved from the Protein Data Bank (PDB code: 1HAO). [Retrieved from [46]]



This helical model served as the baseline structure for introducing mutations. To manage the complexity, mutations were limited to one or two alterations per sequence relative to the original TBA sequence. This approach generated a library of 990 different sequences. Additionally, the library was supplemented with three sequences that were previously reported in the literature as weak thrombin binders (Table 4):

\_

<sup>&</sup>lt;sup>46</sup> Bini, A., Mascini, M., Mascini, M., & Turner, A. P. <u>Selection of thrombin-binding aptamers by using computational approach for aptasensor application</u>. *Biosensors and Bioelectronics*, **26**(11), 4411-4416 (2011).



Table 4: Comparison of thrombin-binding aptamer (TBA) variants and their mutations.

Aptamer Name	Sequence (5' - 3-)	Mutation(s)	Mutation Position(s)
TBA (Original)	GGT TGG TGT GGT TGG	-	-
Best Aptamer	GGT TTG TGT GGT TAG	$G \rightarrow T$ , $G \rightarrow A$	Positions 5, 14
Medium Aptamer	GGC TGG TGT GAT TGG	T→C, G→A	Positions 3, 11
Worst Aptamer	GGT AGG TGT GGT TGC	T→A, G→C	Positions 4, 15
Sequence "a" (Weak binder) <sup>45</sup>	GGT GGT GGT TGT GGT	$T \rightarrow G$ , $G \rightarrow T$ , etc.	Positions 4, 6, 7, 10, 13, 15
Sequence "b" (Weak binder) <sup>46</sup>	GGT AGG GTC GGA TGG	T→A, T→G, etc.	Positions 4, 7, 8, 9, 12
Sequence "c" (Weak binder) <sup>46</sup>	GGT AGG GCA GGT TGG	$T \rightarrow A, T \rightarrow G, G \rightarrow C, T \rightarrow A$	Positions 4, 7, 8, 9
iso-rTBA <sup>47</sup>	GGU UGG UGU GGU UGG	-	-
iso-rTBA:cRNA <sup>47</sup>	CCA ACC ACA CCA ACC	-	-

**Note**: This table presents the original TBA sequence alongside mutated variants. Each modified sequence includes one or two nucleotide substitutions to evaluate changes in thrombin-binding affinity. The "Best," "Medium," and "Worst" aptamers were computationally identified, while sequences "a," "b," and "c" were previously reported in the literature as weak thrombin binders.

- Sequence "a": Contains six mutations (T4G, G6T, T7G, G10T, T13G, G15T) relative to TBA. Its sequence is 5'-GGT GGT GGT TGT GGT-3', as described by Bock et al. (1992).<sup>48</sup>
- **Sequence "b"**: Contains five mutations (T4A, T7G, G8T, T9C, T12A) relative to TBA. Its sequence is 5'-GGT AGG GTC GGA TGG-3', as reported by Tasset et al. (1997).<sup>49</sup>
- **Sequence "c"**: Contains four mutations (T4A, T7G, G8C, T9A) relative to TBA. Its sequence is 5'-GGT AGG GCA GGT TGG-3', also reported by Tasset et al. (1997).<sup>3</sup>

For the simulation, we utilized Apta-MCTS, a Monte Carlo tree search-based approach, to predict aptamer sequences that can potentially bind to the thrombin (P00734) protein. The model configuration included 50 candidate sequences with a length of 30 base pairs, iterated 100 times, and evaluated using a classifier-based scoring function. The candidate aptamer sequences were assessed based on their predicted binding affinity, secondary structure stability, and minimum free energy (MFE). The top-ranked sequences were then shortlisted based on their calculated scores (Table 5).

To determine the similarity scores for potential aptamer sequences we expect, we employed a sequence similarity assessment method, specifically using pairwise sequence comparison algorithm, SequenceMatcher from the difflib library. The similarity score between an expected target aptamer

<sup>&</sup>lt;sup>47</sup> Wagh, A. A., Kumar, V. A., Ravindranathan, S., & Fernandes, M. (2023). <u>Unlike RNA-TBA (rTBA), iso-rTBA, the 2'-5'-linked RNA-thrombin-binding aptamer, is a functional equivalent of TBA. Chemical Communications</u>, **59**(11), 1461-1464.

<sup>&</sup>lt;sup>48</sup> Bock, L. C., Griffin, L. C., Latham, J. A., Vermaas, E. H., & Toole, J. J. <u>Selection of single-stranded DNA molecules that bind and inhibit human</u> thrombin. *Nature*, **355**(6360), 564-566 (1992).

<sup>&</sup>lt;sup>49</sup> Tasset, D. M., Kubik, M. F., & Steiner, W. (1997). <u>Oligonucleotide inhibitors of human thrombin that bind distinct epitopes</u>. *Journal of Molecular Biology*, **272**(5), 688-698 (1997).



(e.g., rTBA, iso-rTBA, or other known aptamer motifs) and the candidate sequences was calculated as follows:

- Pairwise Alignment: Each candidate sequence was compared to the reference aptamer sequence using sequence alignment techniques.
- Similarity Calculation: The similarity ratio was computed as:

$$Similarity \, Score = \frac{Number \, of \, Matching \, Bases}{Total \, Bases \, in \, Reference \, Sequence}$$

where higher values indicate greater resemblance to the expected aptamer.

• Ranking Candidates: Sequences with the highest similarity to known aptamers were prioritized for further validation.

**Table 5** provides the best-matching sequences from the Apta-MCTS-generated candidates based on their similarity scores to the aptamer sequences, including TBA DNA aptamer, iso-rTBA, and iso-rTBA:cRNA. Each row presents the aptamer type, the best-matching candidate sequence, and its computed similarity score. Higher similarity scores indicate a closer structural resemblance to the expected aptamer sequences, suggesting a stronger potential for effective binding.

Table 5: Comparison of Apta-MCTS generated sequences with TBA-variants aptamers based on similarity scores – for the case of the P00734 protein target.

	Best Matching Sequence (from Apta-MCTS Generated Sequences)	Similarity Score
TBA	CAAGAGGUCGGGCUAGCGAAGUGGAGCUUG	0.400
iso-rTBA		0.577
130 112/1		0.577
iso-rTBA:cRNA	CCGGAGGUACGCCUGCACUAGGCAUUAUCC	0.622
ISO-LI RA:CKNA	CCGGAGGUACGCCUGCACUAGGCAUUAUCC	0.622

We generated a set of candidate aptamer sequences with high interaction scores and secondary structures for the for P00734 protein target, with the Apta-MCTS model settings (MCC: 0.607, PPV: 0.696, ACC: 0.777, SN: 0.982, SP: 0.571, NPV: 0.970, YD: 0.554 (173 trees)). The top candidates include:

#### 1. CCGGAGGUACGCCUGCACUAGGCAUUAUCC

- Similarity Score: 0.6222
- Secondary Structure: ..(((....(((((...)))))....)))
- Minimum Free Energy (MFE): -7.19 kcal/mol

#### 2. CCGCGGGAAAACGCCUGCACUAGGCAUUCA

- Similarity Score: 0.5777
- Secondary Structure: ..(((((.....)))))......
- Minimum Free Energy (MFE): -7.59 kcal/mol

#### 3. CGGCGGGAAAACGCCUGCACUAGGCAUCC

- Similarity Score: 0.5777
- Secondary Structure: ..(((((.....)))))......
- Minimum Free Energy (MFE): -7.6 kcal/mol



Figure 17 presents an overview of the workflow for predicting aptamer-target binding in the context of TBA using a combination of computational techniques. The candidate sequence with the highest similarity score from AptaMCTS is CCGGAGGUACGCCUGCACUAGGCAUUAUCC, with its secondary structure depicted. The distribution of docking scores indicates the mean docking score of 855.93 and median score of 834.13, suggesting the effectiveness of the model in predicting binding sites within the thrombin sequence.

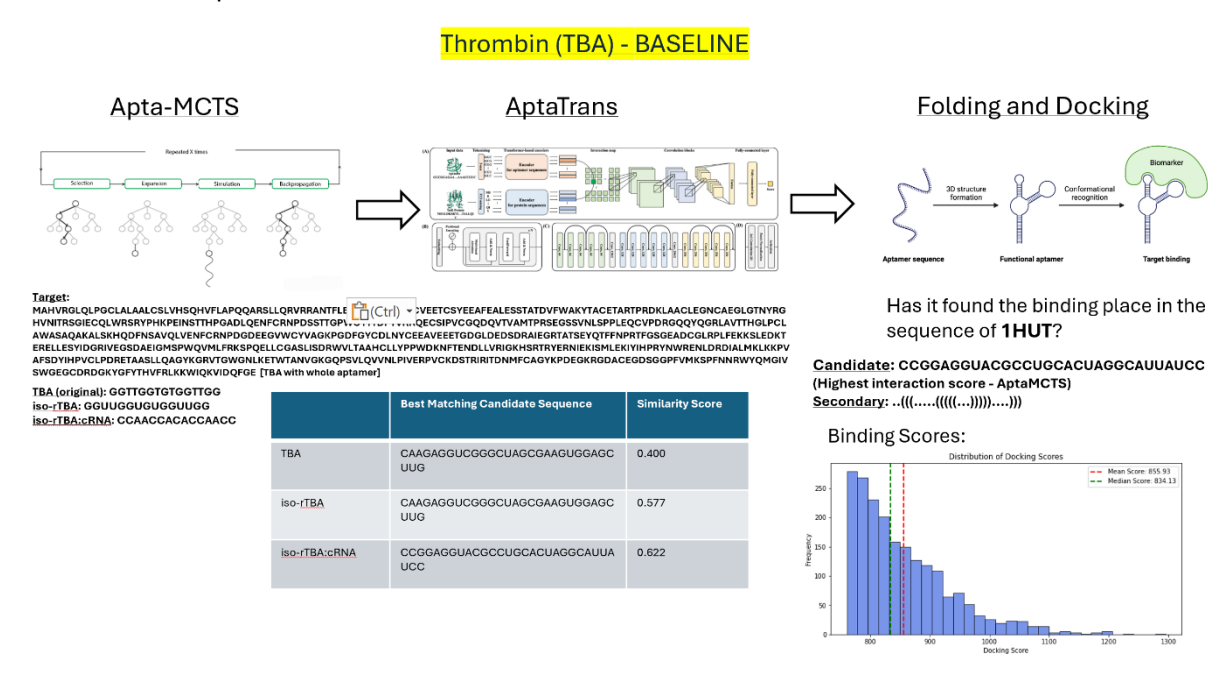


Figure 17: Comparison of models in TBA candidate selection and binding performance.

#### Structure-Guided Aptamer Selection for Beta-amyloid Peptide Sequence

We focused on proposing candidate aptamers by targeting the beta-amyloid peptide sequence, "DAEFRHDSGYEVHHQKLVFFAEDVGSNKGAIIGLMVGGVVIA". The goal was to generate aptamer candidates that could bind to this target, providing a potential tool for AD biomarker detection or therapeutic intervention. Performance metrics and top candidate sequences generated by the Apta-CTS and AptaTrans models are summarized in Table 6.



Table 6: Performance metrics and top candidate sequences for Apta-MCTS models – for the case of the beta-amyloid peptide sequence.

Score Function		Socuences			
Score Function	Top Candidate Scores &				
MCC: 0.484, PPV:	Scores: 0.418,	0.418,	0.418,	0.400,	0.400
1.000, ACC: 0.822,	Sequences:				
SN: 0.290, SP: 1.000,	"CCAUAACAAUUCGUGGCUCU	GCUCCUCGUA",			
NPV: 0.809, YD:	"UGCUAACAAUUCGUGGCUCU	GCUCUGUGGU",			
0.290 (55 trees)	"CUCAUAACAAUUCGUGGCUCI	JGCUCCUCUU",			
	"UGUCCAUGGAAUUCGUGGCU	CUGCUCUUCG",			
	"AAUGUAACAAUUCGUGGCUC	ugcuccucgg"			
MCC: 0.484, PPV:	Scores: 0.5094,	0.4906,	0.4905,	0.4717,	0.4717
1.000, ACC: 0.822,	Sequences:				
SN: 0.290, SP: 1.000,	"AAUCUAGCUCUUGCUGUGGG	ACAAUCGAGC",			
NPV: 0.809, YD:	"CAACUGGACUCGGGCGUUGC	UGUUAACAUA",			
0.290 (53 trees)	"AGCCUGGACUCGGGCGUUGC	UGUUAACAUG",			
	"UUCAUGUGGGACACUGCUGA	UGCACAAAGA",			
	"UGACGAAACAACUGUUGCUG	AGUGGGCCCU"			
MCC: 0.484, PPV:	Scores: 0.5128,	0.4871,	0.4871,	0.4871,	0.4872
1.000, ACC: 0.822,	Sequences:				
SN: 0.290, SP: 1.000,	"CGGAAGCACCCGGGGCGCCCA	AAGGCGGGU",			
NPV: 0.809, YD:	"CUCGGAAGCACCCGGGGCGCC				
0.290 (39 trees)	"AGGGAGUCCCGGGGCGCCCAC	•			
(	"CGGAGGGACCCGGGGCGCCCA	· ·			
	"GGGGGAAGCACCCGGGGCGCG	,			
MCC: 0.484, PPV:	Scores: 0.5428,	0.5428,	0.5428,	0.5428,	0.5142
1.000, ACC: 0.822,	Sequences:	0.0 .20,	0.0 .20,	0.0 .20,	0.01.1
SN: 0.290, SP: 1.000,	"AAGCUGUGCUGUUGCAUGGC	AAAGCCGAHA"			
NPV: 0.809, YD:	"UCGAAGUGCUGUUGCAUGGC				
0.290 (35 trees)	"GAAGUGCUGUUGCAUGGCAA	•			
0.250 (55 trees)	"AAAAGUGCUGUUGCAUGGCA	•			
	"GAAAGUGCUGUUGCAUGGCA	•			
MCC: 0.607, PPV:	Scores: 0.7718,	0.7670,	0.7624,	0.7442,	0.7441
	Sequences:	0.7670,	0.7624,	0.7442,	0.7441
0.696, ACC: 0.777,		CHACALICCLIC"			
SN: 0.982, SP: 0.571, NPV: 0.970, YD:	"CCUCCUUUACUCCCGAUGCCG				
0.554 (173 trees)	"CUUAGCCUUACGAUGACACU	,			
0.554 (173 trees)	"UUUUGAUUCUUCCAUUGACG	•			
	"UCGUACAUCACUUUUUAUGG				
1466: 0.607 PDV	"UUCCACCAUAGCUCGGUAUGA		0.0267	0.0360	0.0260
MCC: 0.607, PPV:	Scores: 0.8549,	0.8545,	0.8367,	0.8368,	0.8368
0.696, ACC: 0.777,	Sequences:				
SN: 0.982, SP:	"GGGCACCCGAGGAACCGCGA	•	"UUAGACCUGC	GUGCACCGGUAC	UUGGAUA",
0.571, NPV: 0.970,	"CCGCGAGGAUCGAACACCGU	•			
YD: 0.554 (49 trees)	"GCGCGGUAUCCUGACCACCG				
	"ACGAUCCUGACCACCGUUUCI	JGAACGGUUG"			
MCC: 0.484, PPV:	Scores: 0.4545,	0.4545,	0.4545,	0.4415,	0.4415
1.000, ACC: 0.822,	Sequences:				
SN: 0.290, SP: 1.000,	"GUAUCUUAAGGAAAACAAAG	AGCCAAAAUC",			
NPV: 0.809, YD:	"UCUGAACUUAAAACAAAGACI	JACCUUGGUA",			
0.290 (77 trees)	"UGACUUAAAACAAAGACUAC	CUUGGUGAAU",			
	"AGUAUCUUAAAACAAAGAUU	AUAUGGAAGU",			
	"AUUUCUUAAACAAAGACUUG	GCAGLIGAGGG"			



We generated a set of candidate aptamer sequences with high interaction scores and secondary structures for the for the case of the beta-amyloid peptide sequence (MCC: 0.607, PPV: 0.696, ACC: 0.777, SN: 0.982, SP: 0.571, NPV: 0.970, YD: 0.554 (49 trees)). The top candidates include:

#### 1. GGGCACCCGAGGAACCGCGACUGCAUGUCG

• Interaction Score: 0.8549

• Secondary Structure: .((..((...))..)).((((....))))

Minimum Free Energy (MFE): -5.19 kcal/mol

#### 2. UUAGACCUGCGUGCACCGGUACUUGGAUAC

• Interaction Score: 0.8546

• Secondary Structure: .....(((.((((...)))).)))....

• Minimum Free Energy (MFE): -3.79 kcal/mol

#### 3. CCGCGAGGAUCGAACACCGUCGCAACUUGA

• Interaction Score: 0.8367

• Secondary Structure: ..((((((......)).)))).......

• Minimum Free Energy (MFE): -6.90 kcal/mol

#### 4. GCGCGGUAUCCUGACCACCGUUUCUGUAAA

Interaction Score: 0.8367

• Secondary Structure: .(((((......)))))........

• Minimum Free Energy (MFE): -4.40 kcal/mol

#### 5. ACGAUCCUGACCACCGUUUCUGAACGGUUG

• Interaction Score: 0.8367

• Secondary Structure: .....(((((((...))))))...

• Minimum Free Energy (MFE): -5.69 kcal/mol

These sequences represent promising initial candidates for binding to the Beta-amyloid Peptide target, providing a solid foundation for further refinement and validation. To optimize candidate selection, we performed Apta-Trans simulations using the highest-ranked sequences generated by Apta-MCTS as input. Table 7 summarizes the performance metrics and highlights the top candidate sequences identified by both the Apta-MCTS (Machine Learning) and Apta-Trans (Deep Learning) models for the Beta-amyloid Peptide target.

Table 7: Interaction scores and top candidate sequences of Apta-MCTS (Machine learning) and AptaTrans (Deep learning) models for Beta-amyloid Peptide target.

Apta-MCTS <sup>39</sup>	AptaTrans <sup>38</sup>
Candidate:	Candidate:
GGGCACCCGAGGAACCGCGACUG	CUCUUAUCAGGCGUAUUUUGGGCGUCUCAGGA
CAUGUCG	UAUGAGUG
Interaction Score: 0.8549	Interaction Score: 0.7623

The Apta-MCTS model outperforms AptaTrans for the Beta-amyloid Peptide target, with a higher interaction score (0.8549 vs. 0.7623), suggesting its greater effectiveness in identifying strong-binding



candidate sequences in this case. In addition, Figure 18 presents the performance metrics and top candidate sequences identified by both the Apta-MCTS (Machine Learning) and AptaTrans (Deep Learning) models for beta-amyloid peptide binding. The final folding and docking analysis assesses the binding capability of the highest-scoring candidate from Apta-MCTS within the full 1IYT sequence. The secondary structure prediction is also provided for the selected candidate. The distribution of docking scores indicates a mean binding score of 5149.79, with a median score of 5023.2, demonstrating the relative efficiency of the optimized aptamers in binding to the beta-amyloid peptide.

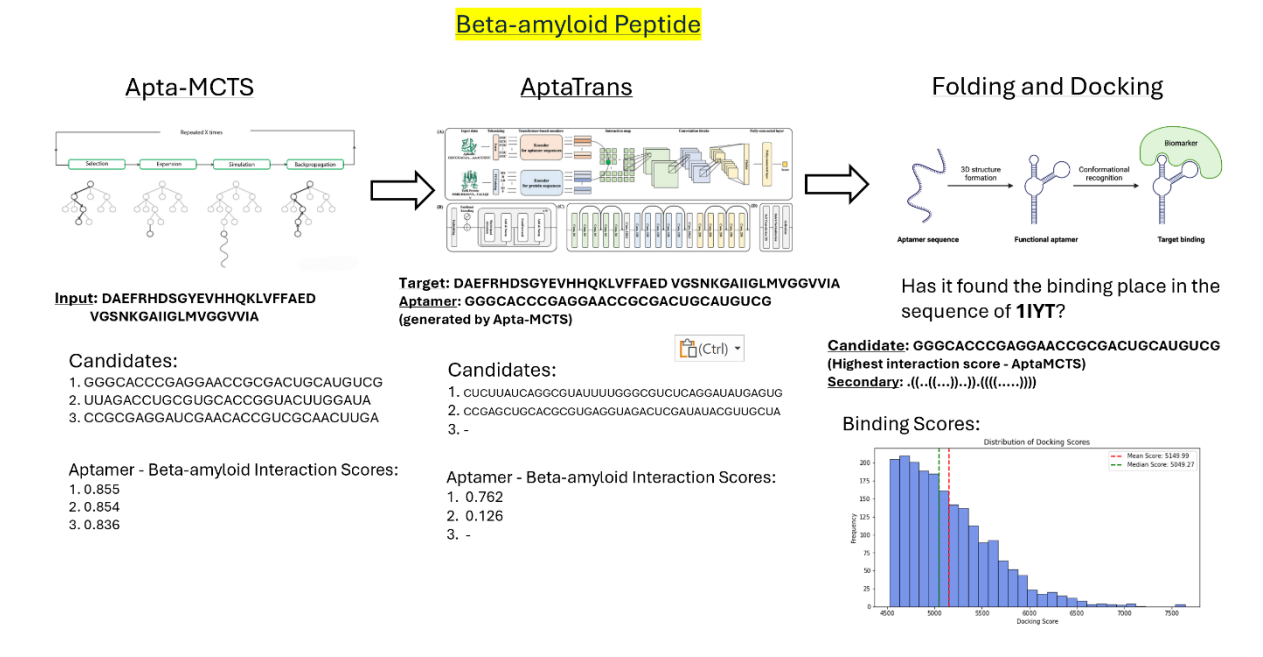


Figure 18: Comparison of Apta-MCTS and AptaTrans models in Beta-Amyloid Peptide candidate selection and binding performance.

#### Structure-Guided Aptamer Selection for Beta-amyloid pTau-217 Sequence

We focused on proposing candidate aptamers by targeting the partial of **pTau-217** sequence<sup>50</sup>. To achieve this, we employed computational approaches using the Apta-MCTS and AptaTrans models for API prediction. **Table 8** presents the performance metrics and top candidate sequences generated by the Apta-MCTS models. The highest-ranked sequences, consistently identified across multiple runs, exhibited binding potential to the pTau-217 target, highlighting the model's effectiveness in aptamer selection.

\_

<sup>&</sup>lt;sup>50</sup> See Appendix II



# Table 8: Performance metrics and top candidate sequences for Apta-MCTS models – for the case of the partial of the pTau-217 sequence.

Score Function		date Scores 8	2 Sequences			
MCC: 0.484, PPV: 1.000, ACC:	Scores:	0.418,	0.418,	0.418,	0.400,	0.400
0.822, SN: 0.290, SP: 1.000,	Sequences:		_			
NPV: 0.809, YD: 0.290 (55			ACAAUAUUCCU",			
trees)			AUAUUCCCGAG",			
			CAAUAUUAACC",			
			CAAUAUUAGGA",			
	"GCGAUCGA	ACUUGCCAGCC	UACAAUAUUCC"			
MCC: 0.484, PPV: 1.000, ACC:	Scores:	0.4528,	0.4528,	0.4339,	0.4339,	0.4339
0.822, SN: 0.290, SP: 1.000,	Sequences:					
NPV: 0.809, YD: 0.290 (53	"CAUCUUUA	AGAUGCAAUCC	CGGGACGGGUC",			
trees)	"CUAUCUUU	AAGAUGCAAUC	CCGGGACGGGC",			
	"AUCACUUA	AGAUGCAAUCC	CGGGACGUGUG",			
	"UUGUUUAA	GAUGCAAUCCC	GGGACGUUACU",			
	"CCUCUUUA	AGAUGCAAUCC	CGGGACGGGUA"			
MCC: 0.484, PPV: 1.000, ACC:	Scores:	0.6923,	0.6923,	0.6923,	0.6923,	0.6923
0.822, SN: 0.290, SP: 1.000,	Sequences:					
NPV: 0.809, YD: 0.290 (39	"AAAAUCGG	UCAUGAGUCGL	IAUAGUCUAUGA",			
trees)	"AGAUCGGU	CAUGAGUCGUA	AUAGUCUAUCUU",			
	"CAAUCGGU	CAUGAGUCGUA	UAGUCUAUGCC",			
	"AAAAUCGG	UCAUGAGUCGL	IAUAGUCUAUGU",			
	"UAGAUCGG	UCAUGAGUCGL	JAUAGUCUAUGC"			
MCC: 0.484, PPV: 1.000, ACC:	Scores:	0.5428,	0.5142,	0.5142,	0.5142,	0.5142
0.822, SN: 0.290, SP: 1.000,	Sequences:					
NPV: 0.809, YD: 0.290 (35	"GACGGGUA	UACUGUGGUUI	JUAAUGCGAGCG",			
trees)	"ACGUAUAC	JGUGGUUUUA	AUGCGAGCGAAA",			
	"ACUGGGUA	UACUGUGGUUI	JUAAUGCGAGCA",			
	"ACUGGGUA	UACUGUGGUUI	JUAAUGCGAGCC",			
	"GCAUCAUA	CUGUGGUUUUA	AAUGCGAGCACA"			
MCC: 0.607, PPV: 0.696, ACC:	Scores:	0.8456,	0.8421,	0.8409,	0.8409,	0.8409
0.777, SN: 0.982, SP: 0.571,	Sequences:					
NPV: 0.970, YD: 0.554 (173	"CAUGAUUA	CCCCUCUCCAC	UUUCCGGGUAG",			
trees)	"CUGUUACC	CUCUCCACUUG	CCUUAUUGCAC",			
	"CUUACCCU	CUCCACUUGCC	UUAUUGCCAUG",			
	"CUUACCCU	CUCCACUUGCC	UUAUUGCAUGA",			
	"GAGUACCC	UCUCCACUUGC	CUUAUUGCCAC"			
MCC: 0.607, PPV: 0.696, ACC:	Scores:	0.8966,	0.8966,	0.8966,	0.8966,	0.8966
0.777, SN: 0.982, SP: 0.571,	Sequences:					
NPV: 0.970, YD: 0.554 (49	"GACGGCACI	JGGCGGGAGAU	IGAUGCGACAGG",			
trees)	"ACUCCUGC	GGCACUGGCGG	GAGAUGAUCAC",			
	"GCGAUGCG	GCACUGGCGGG	AGAUGAUCAGG",			
	"CACUCUGC	GGCACUGGCGG	GAGAUGAUCGG",			
	"ACUCACUG	CGGCACUGGCG	GGAGAUGAUAG"			
MCC: 0.484, PPV: 1.000, ACC:	Scores:	0.5064,	0.4935,	0.4675,	0.4675,	0.4675
0.822, SN: 0.290, SP: 1.000,	Sequences:					
NPV: 0.809, YD: 0.290 (77	"CCAUGUGU	GUGGGUUGUG	GGCGUUUAGGAU",			
trees)	"GCAUGUGU	guggguugug	GGCGUUUAGGGC",			
	"CAUCAUGU	GUGUGGGUUG	UGGGCGUUUAAA",			
			GGCGUUUAUAAU",			
			GGGCGUUUAUGA"			



We generated a set of candidate aptamer sequences with high interaction scores and secondary structures for the case of the partial of the pTau-217 sequence (MCC: 0.607, PPV: 0.696, ACC: 0.777, SN: 0.982, SP: 0.571, NPV: 0.970, YD: 0.554 (49 trees)). The top candidates include:

#### 1. GACGGCACUGGCGGGAGAUGAUGCGACAGG

- Interaction Score: 0.8966
- Secondary Structure: ......(((.((.(.(....).)).))).
- Minimum Free Energy (MFE): -3.5 kcal/mol

#### 2. ACUCCUGCGGCACUGGCGGGAGAUGAUCAC

- Interaction Score: 0.8966
- Secondary Structure: .(((((((.....))))))).......
- Minimum Free Energy (MFE): -12.19 kcal/mol

#### 3. GCGAUGCGGCACUGGCGGGAGAUGAUCAGG

- Interaction Score: 0.8966
- Secondary Structure: ((.....)).(((((((....)).)))).
- Minimum Free Energy (MFE): -4.80 kcal/mol

#### 4. CACUCUGCGGCACUGGCGGGAGAUGAUCGG

- Interaction Score: 0.8966
- Secondary Structure: ((.(((.(.(...)).).)))).....
- Minimum Free Energy (MFE): -7.0 kcal/mol

#### 5. ACUCACUGCGGCACUGGCGGGAGAUGAUAG

- Interaction Score: 0.8966
- Secondary Structure: .(((.((((.....)))))))......
- Minimum Free Energy (MFE): -8.39 kcal/mol

AptaTrans could not be applied due to the absence of ptau-217 target information in the dataset, as its training data lacked the relevant kmers. Consequently, AptaTrans assigns a near-zero score, signaling a warning message that it is not suitable for this case in the interference simulation.

#### Structure-Guided Aptamer Selection for Beta-amyloid GFAP Sequence

We aimed to identify candidate aptamers targeting the GFAP sequences, provided by Novaptech. Tables 9 and 10 summarize the performance metrics and ranking sequences generated by the Apta-MCTS models. The evaluation employed MCC, PPV, ACC, SN, SP, NPV, and YD to assess model performance across different tree depths. The highest-scoring sequences, consistently identified across multiple runs, exhibited strong potential for binding to the GFAP target, highlighting the model's reliability in aptamer selection.



# Table 9: Performance metrics and top candidate sequences for Apta-MCTS models – for the case of the partial of the FIB012B - GFAP sequence.

Coore Eupotion	Ton Cand	idata Scarac	2 Coguences	ence.				
Score Function			& Sequences					
MCC: 0.484, PPV: 1.000, ACC:	Scores:	0.4363,	0.4181,	0.4181,	0.3818,	0.3818		
0.822, SN: 0.290, SP: 1.000,	Sequences:							
NPV: 0.809, YD: 0.290 (55	"GUUCUUCGAUAAGUCCUCUCGAGACAUCAU",							
trees)	"CGUGAACUUAUUCCUCCAGAGGACUCUAUC",							
	"CGCAUGGI	"CGCAUGGUGGGUCCUCUUAUCGCUGGUAAG",						
	"AGGAGUG	"AGGAGUGUUACUUCGUCCUCUAGACGGUUG",						
	"GUGGGGG	GUUCUUCGUC	CUCUAAUUUAUA	AG"				
MCC: 0.484, PPV: 1.000, ACC:	Scores:	0.4150,	0.4150,	0.4150,	0.3962,	0.3962		
0.822, SN: 0.290, SP: 1.000,	Sequences:	Sequences:						
NPV: 0.809, YD: 0.290 (53	"AUGCCUAL	"AUGCCUAUUCGCAGCUUUGGAACGCUUCUU",						
trees)	"GGAUGCA	AGGACAAGGCA	GCUUUGAAGCU	G" <i>,</i>				
	"CUGGGCU	AGGGCAGGCAG	CUUUGAUCUUC	U",				
	"ACGUGGG	CAGCUUUGUCC	CCGGCAAUCUCGA	۹",				
	"GUGAGGG	UCCUCGCAGCL	IUUGCAGAUUGG	iC"				
MCC: 0.484, PPV: 1.000, ACC:	Scores:	0.4615,	0.4615,	0.4615,	0.4615,	0.4358		
0.822, SN: 0.290, SP: 1.000,	Sequences:							
NPV: 0.809, YD: 0.290 (39	"AUGAAGA	ACGCAAGAGCA	UAUGGAAAAUCA	۹",				
trees)	"AAGAGAA(	CGCAAGAGCAU	AUGGAAAAUGU	۹",				
	"GUUCAAG	AACGCAAGAGC	AUAUGGAAAAU	Ξ",				
	"GAGAACG(	CAAGAGCAUAU	GGAAAAUGUCU	Α",				
			AUGGAAAAUGU					
MCC: 0.484, PPV: 1.000, ACC:	Scores:	0.4571,	0.4285,	0.4285,	0.4285,	0.4000		
0.822, SN: 0.290, SP: 1.000,	Sequences:	,	,	•	•			
NPV: 0.809, YD: 0.290 (35	•	"GGUAGACCUAGAUUGUCUACUAUCUGGGUA",						
trees)		"UAUCUUCCGUUUAGUCUAUGUCGACGACGU",						
,		"UAUACCACUUUACUAGUCUGUGUGGCCCCA",						
			JGUCUAACGUCG	•				
	"GGACCCGL	JUCCGAACCCA	CUGGCAAGUUGC	, ,				
MCC: 0.607, PPV: 0.696, ACC:	Scores:	0.7559,	0.7552,	0.7549,	0.7541,	0.7490		
0.777, SN: 0.982, SP: 0.571,	Sequences:	•	·	·	•			
NPV: 0.970, YD: 0.554 (173	•		ACACCCCGGGGA	۸",				
trees)	"CCGAAACO	GAUCCACUGO	GACACCCGCUCA	",				
,			CACCCCGGCCCG	•				
			CACCCCGGUACA					
	"UUCAACCO	GAUCCACUGCG	ACACCCCGGCAC	n .				
MCC: 0.607, PPV: 0.696, ACC:	Scores:	0.7505,	0.7395,	0.7125,	0.7118,	0.6991		
0.777, SN: 0.982, SP: 0.571,	Sequences:	,	,	-,	-,			
	"GCCGGGCGUCCUAACAGCCUUGCCGACUCG",							
NPV: 0.9/0. YD: 0.554 149	"GCCGGGCGUCCUAACAGCCUUGCCGACUCG",  "GCGGUAGCGAACAGUGACCCUGGGGCUACC",							
NPV: 0.970, YD: 0.554 (49 trees)		CGAACAGUGAC	CCUGGGGCUAC	~II				
trees)	"GCGGUAG			•				
	"GCGGUAG( "GCGGGCCL	JUUGACAACAG	CCAGCACCCUGA	",				
	"GCGGUAGO "GCGGGCCU "ACCCCCGG	JUUGACAACAG JUAGCCCUAACA	CCAGCACCCUGA AGCCGACUUAGA'					
trees)	"GCGGUAGO "GCGGGCCU "ACCCCCGG "GGCGCACC	JUUGACAACAG JUAGCCCUAACA CCUAACAGCCAA	CCAGCACCCUGA AGCCGACUUAGA AACCAGGGCGGA	 	0.3376	0.3376		
MCC: 0.484, PPV: 1.000, ACC:	"GCGGUAGG "GCGGGCCL "ACCCCCGG "GGCGCACC	JUUGACAACAG JUAGCCCUAACA	CCAGCACCCUGA AGCCGACUUAGA'		0.3376,	0.3376		
MCC: 0.484, PPV: 1.000, ACC: 0.822, SN: 0.290, SP: 1.000,	"GCGGUAGG "GCGGGCCC "ACCCCCGG "GGCGCACC Scores: Sequences:	JUUGACAACAG JUAGCCCUAACA CCUAACAGCCAA 0.3896,	CCAGCACCCUGA AGCCGACUUAGA AACCAGGGCGGA 0.3636,	0.3506,	0.3376,	0.3376		
MCC: 0.484, PPV: 1.000, ACC: 0.822, SN: 0.290, SP: 1.000, NPV: 0.809, YD: 0.290 (77	"GCGGUAGG "GCGGGCCL "ACCCCCGG "GGCGCACC Scores: Sequences:	JUUGACAACAG JUAGCCCUAACA CCUAACAGCCAA 0.3896, CGAUUCGGGUA	CCAGCACCCUGA AGCCGACUUAGA' AACCAGGGCGGA' 0.3636, AGGACUUCAAAA	0.3506, U",	0.3376,	0.3376		
MCC: 0.484, PPV: 1.000, ACC: 0.822, SN: 0.290, SP: 1.000,	"GCGGUAGG "GCGGGCCL "ACCCCCGG "GGCGCACC Scores: Sequences: "GGAGCAGG	JUUGACAACAG JUAGCCCUAACA CCUAACAGCCAA 0.3896, CGAUUCGGGUA JACGUAGGGUA	CCAGCACCCUGA AGCCGACUUAGA AACCAGGGCGGA 0.3636, AGGACUUCAAAA ACGAUUUGCCUA	0.3506, U",	0.3376,	0.3376		
MCC: 0.484, PPV: 1.000, ACC: 0.822, SN: 0.290, SP: 1.000, NPV: 0.809, YD: 0.290 (77	"GCGGUAGG" "GCGGGCCC" "ACCCCCGG" "GGCGCACC" Scores: Sequences: "GGAGCAGG" "AUACCCGC"	JUUGACAACAG JUAGCCCUAACA CCUAACAGCCAA 0.3896, CGAUUCGGGUA JACGUAGGGUA UACUCGGGUAC	CCAGCACCCUGA AGCCGACUUAGA AACCAGGGCGGA  0.3636, AGGACUUCAAAA AGGACUUCAAAAA	0.3506, U", A",	0.3376,	0.3376		
MCC: 0.484, PPV: 1.000, ACC: 0.822, SN: 0.290, SP: 1.000, NPV: 0.809, YD: 0.290 (77	"GCGGUAGG "GCGGGCCL "ACCCCCGG "GGCGCACC Scores: Sequences: "GGAGCAGG "AUACCCGL "GGAUUCG	JUUGACAACAG GUAGCCCUAACA CCUAACAGCCAA  0.3896, CGAUUCGGGUA JACGUAGGGUA UACUCGGGUAC	CCAGCACCCUGA AGCCGACUUAGA AACCAGGGCGGA 0.3636, AGGACUUCAAAA ACGAUUUGCCUA	", " 0.3506, U", A", U",	0.3376,	0.3376		



# Table 10: Performance metrics and top candidate sequences for Apta-MCTS models – for the case of the partial of the FIB001C - GFAP sequence.

Score Function	•	date Scores	& Sequences					
MCC: 0.484, PPV: 1.000, ACC:	Scores:	0.4545,	0.3818,	0.3636,	0.3454,	0.3454		
0.822, SN: 0.290, SP: 1.000,	Sequences:	00 .0,	0.0020,	0.0000,	0.0 .0 .,	0.0 .0 .		
NPV: 0.809, YD: 0.290 (55	•	CCUGCAGCGA	AGGUGUGAGGGL	J".				
trees)	"AACAUGGGGACAGCGUAGAGCCUGCGGAU",							
	"CUUUUGUGCUUGAGGACGGACUUGACUGAU",							
	"GCACUAACAUGGCUAGGGAGGAGCAUCG",							
			GGCACCUCUAGAC	Ť				
MCC: 0.484, PPV: 1.000, ACC:	Scores:	0.4339,	0.4339,	0.4339,	0.4150,	0.4150		
0.822, SN: 0.290, SP: 1.000,	Sequences:	0000,	0. 1000,	01.000,	0200,	0200		
NPV: 0.809, YD: 0.290 (53	•	'CUCCUUCCUUUUCCCCGGCCCGGCCGCCG",						
trees)		"ACGCUUGCUGGUCCGACUAUUUGCAUGCUU",						
			CUAUUUGCAUGGI	•				
			CCGGGGGGAGUA	•				
			ACUAUUUGCAUG(	•				
MCC: 0.484, PPV: 1.000, ACC:	Scores:	0.3589,	0.3589,	0.3589,	0.3589,	0.3589		
0.822, SN: 0.290, SP: 1.000,	Sequences:	0.5505,	3.3303,	0.5505,	2.3333,	3.5565		
NPV: 0.809, YD: 0.290 (39	·	บดดดดดดดดดดดดดดดดดดดดดดดดดดดดดดดดดดดดดด	GACGAUUCCCGGA	"				
trees)			JUGCUCUCAUAAL					
1.003)			GCGGCGUUCCUGG	,				
			JCGAUAUGUCUG <i>I</i>	•				
			ACGGAGGAGGUA	•				
MCC: 0.484, PPV: 1.000, ACC:	Scores:	0.4285,	0.4000,	0.4000,	0.4000,	0.4000		
0.822, SN: 0.290, SP: 1.000,	Sequences:	0.4205,	0.4000,	0.4000,	0.4000,	0.4000		
NPV: 0.809, YD: 0.290 (35	•	GUGCUUUCU	GUUAGGGACCAG	Δ"				
trees)			JCUUUGUGGACAL	•				
1.003)			GGUUGGAAAAUU(	ŕ				
			CGAUCCGAAGAAA	•				
			UUGCCGGACGAA					
MCC: 0.607, PPV: 0.696, ACC:	Scores:	0.7094,	0.7079,	0.7029,	0.6961,	0.6890		
0.777, SN: 0.982, SP: 0.571,	Sequences:	0.705 1,	0.7073,	0.7023,	0.0301,	0.0050		
NPV: 0.970, YD: 0.554 (173		GUGCGAACAG	GUAGUCCCCCGGC					
trees)			AACAUCGCCUAGA	•				
1.003)			ACAGUACCGCUG'	•				
			CCGUUCGGGUCA'	•				
			GUAGUUACAUUU	•				
MCC: 0.607, PPV: 0.696, ACC:	Scores:	0.8302,	0.8138,	0.8110,	0.8110,	0.8108		
0.777, SN: 0.982, SP: 0.571,	Sequences:		,		,	3.0200		
NPV: 0.970, YD: 0.554 (49	•	UACCCCCGCC	GAUAACGGGCGA	<b>."</b> ,				
trees)			GAUAAACUUGCC	•				
•			CGCCGAUAAACCU	•				
	"CCGGGGACUACCCCGCCGAUAAAGCGGGC",							
	"CAUGCGGACUACCCCCGCCGAUAAACGGGC"							
MCC: 0.484, PPV: 1.000, ACC:	Scores:	0.3506,	0.3506,	0.3246,	0.3246,	0.3246		
0.822, SN: 0.290, SP: 1.000,	Sequences:							
NPV: 0.809, YD: 0.290 (77		AGGGUAGGU	UCUGACGAUUAA	U",				
trees)	"AUGGGUUC	CUGAAUGGU	UCUCGCGAUUGA	A",				
	"AAGAGCUG	UGUGCGAACA	ACGUGUGUCUGC	C",				
	"UGGUGUUC	CUGUGGCUCC	UAACUCGCAGGAG	G",				
"GAUCAUUUGGGCAUCGGUUACGUUAUGUCA"								



We generated a set of candidate aptamer sequences with high interaction scores and secondary structures for the for the case of the FIB001C - GFAP sequence (MCC: 0.607, PPV: 0.696, ACC: 0.777, SN: 0.982, SP: 0.571, NPV: 0.970, YD: 0.554 (49 trees)). The top candidates include:

1	LICCAGG	ACHAC	CCCCC	CCCALIA	ACGGGCGA
т.	UGCAGG	ALUAL		CCGAUA	ACGGGCGA

- Interaction Score: 0.8302
- Secondary Structure: ....((.....))((((......)))).
- Minimum Free Energy (MFE): -7.4 kcal/mol

#### 2. ACUAUGACUACCCCGCCGAUAAACUUGCC

- Interaction Score: 0.8138
- Secondary Structure: .....
- Minimum Free Energy (MFE): 0.0 kcal/mol

#### 3. UGGAGCGGACUACCCCCGCCGAUAAACCU

- Interaction Score: 0.8110
- Secondary Structure: ..(.(((((.....))))))........
- Minimum Free Energy (MFE): -9.60 kcal/mol

#### 4. CCGGGGACUACCCCCGCCGAUAAAGCGGGC

- Interaction Score: 0.8110
- Secondary Structure: .(((((.....)))))(((.....)))..
- Minimum Free Energy (MFE): -11.8 kcal/mol

#### 5. CAUGCGGACUACCCCCGCCGAUAAACGGGC

- Interaction Score: 0.8108
- Secondary Structure: ...((((.....))))......
- Minimum Free Energy (MFE): -5.40 kcal/mol

In addition, we generated a set of candidate aptamer sequences with high interaction scores and secondary structures for the for the case of the FIB012B - GFAP sequence (MCC: 0.607, PPV: 0.696, ACC: 0.777, SN: 0.982, SP: 0.571, NPV: 0.970, YD: 0.554 (173 trees)). The top candidates include:

#### 1. GCAGACCGAUCCACUGCGACACCCCGGGGA

- Interaction Score: 0.7559
- Secondary Structure: ((((......))))......
- Minimum Free Energy (MFE): -4.0 kcal/mol

#### 2. CCGAAACCGAUCCACUGCGACACCCGCUCA

- Interaction Score: 0.7552
- Secondary Structure: .....(((....)))...
- Minimum Free Energy (MFE): -2.79 kcal/mol

#### 3. UUGACCGAUCCACUGCGACACCCCGGCCCG

- Interaction Score: 0.7549
- Secondary Structure: ....(((.....)))....
- Minimum Free Energy (MFE): -1.29 kcal/mol

#### 4. GAGACCGAUCCACUGCGACACCCCGGUACA

- Interaction Score: 0.7541
- Secondary Structure: ...((((.....))))...
- Minimum Free Energy (MFE): -3.00 kcal/mol

#### 5. UUCAACCGAUCCACUGCGACACCCCGGCAC

- Interaction Score: 0.7490
- Secondary Structure: .....(((.....(((......))).
- Minimum Free Energy (MFE): -1.70 kcal/mol



AptaTrans was not applicable due to the absence of GFAP target information in the dataset, as its training data lacked the necessary kmers. As a result, AptaTrans assigns a near-zero score, indicating its unsuitability as a warning message for this case in the interference simulation.



## 3. Aptamers' Optimization

Aptamers selection leads to the full-length aptamers. The length of the aptamers can further be decreased which can help in reducing the synthesis cost and facilitate modifications for use as probes on GFET and electrochemical sensors. The process called truncation involves sequential removal of certain portions of full-length aptamers on the basis of conserved motifs and distinct secondary structure elements. Two full-length GFAP aptamers, FIB012B and FIB001C were selected further for length optimization after their kinetics studies. Based on the secondary structure predicted through bioinformatic analysis, three truncated variants of each aptamer were designed, reducing length of FIB012B from 89 nt to 74 nt, 49 nt and 21 nt (T1, T2 and T3, respectively), and length of FIB001C from 80 nt to 57 nt 30 nt and 20 nt (T1, T2 and T3, respectively), as illustrated in the Figure 19.

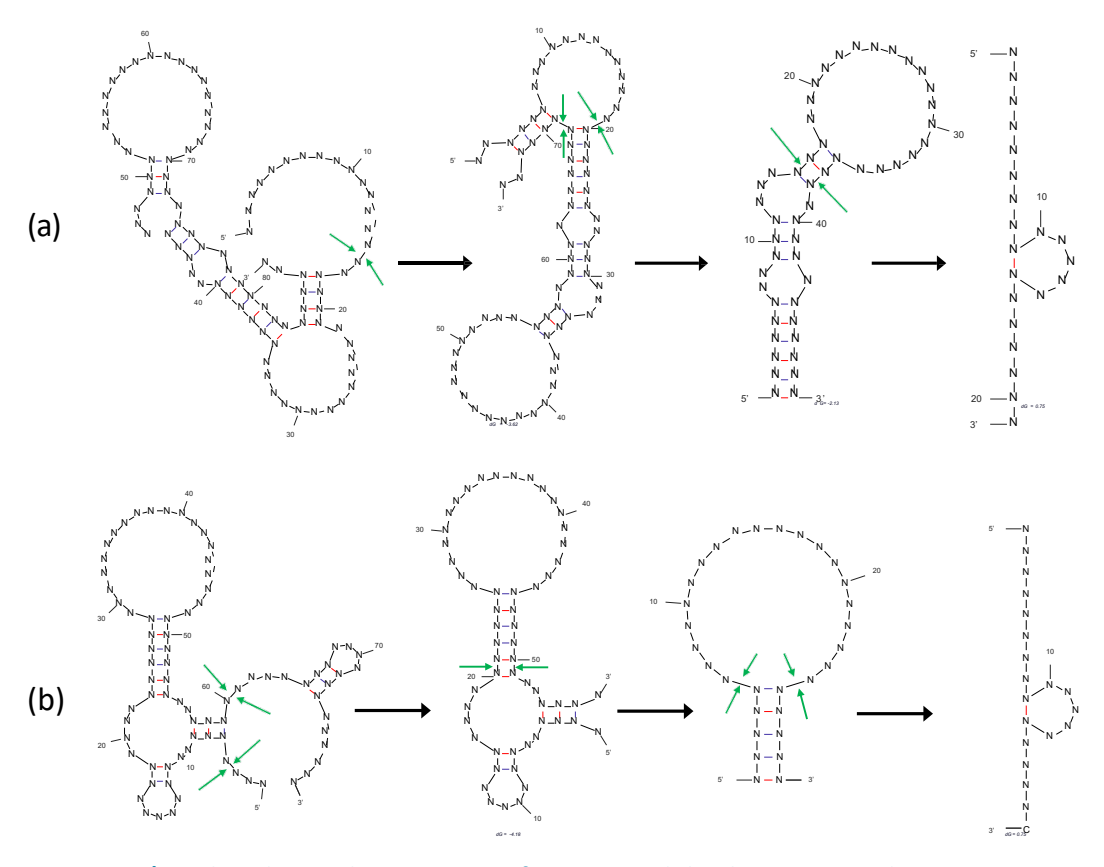


Figure 19: a) Predicted secondary structure of FIB012B and the three truncated variants, FIB012B - T1, T2 and T3; b) Predicted secondary structure of FIB001C and the three truncated variants, FIB001C - T1, T2 and T3. Green arrows indicate the truncation sites. The sequences have been coded.

Following the evaluation of the binding properties of aptamer candidates by SPR, two aptamers were chosen for optimization, i.e.; FIB012B and FIB001C. Based on the secondary structure predicted through bioinformatic analysis, three truncated variants of each aptamer were designed, reducing length of FIB012B from 89 nt to 74 nt, 49 nt and 21 nt (T1, T2 and T3, respectively), and length of FIB001C from 80 nt to 57 nt 30 nt and 20 nt (T1, T2 and T3, respectively), as illustrated in Figure 19.

These truncated variants were tested for their binding with GFAP by SPR. Briefly, biotinylated truncated variants were immobilized on the streptavidin functionalized CM5 sensor chip, and GFAP



solutions were flown over. The unmodified reference cell was used for non-specific binding and blank subtraction. Besides, thrombin aptamer was also used as a control oligo to check non-specific recognition of GFAP.

Further, several concentrations of GFAP (30, 60, 120, 240 and 480 nM) were successively circulated over the aptamers immobilized on the two chips. The binding properties of aptamers were evaluated by single cycle kinetic measurement and analyzed using the 1:1 Langmuir model. A strong and stable binding was detected for all tested truncated aptamers to GFAP. However, the accurate binding parameters couldn't be extracted from the obtained sensorgrams, because the complexes didn't dissociate during the analysis (Figures 20a and 20b). However, it can be observed that all truncated variants of both FIB012B and FIB001C bind to the GFAP and that the aptamer/GFAP complexes are characterized by a K<sub>D</sub> value in the low nanomolar range. Highest signal amplitude was detected for the binding of GFAP to FIB001C-T3 to GFAP. In addition, binding of GFAP to a control aptamer THR002 was negligible (more than 10x lower signal than for FIB001C-T3).

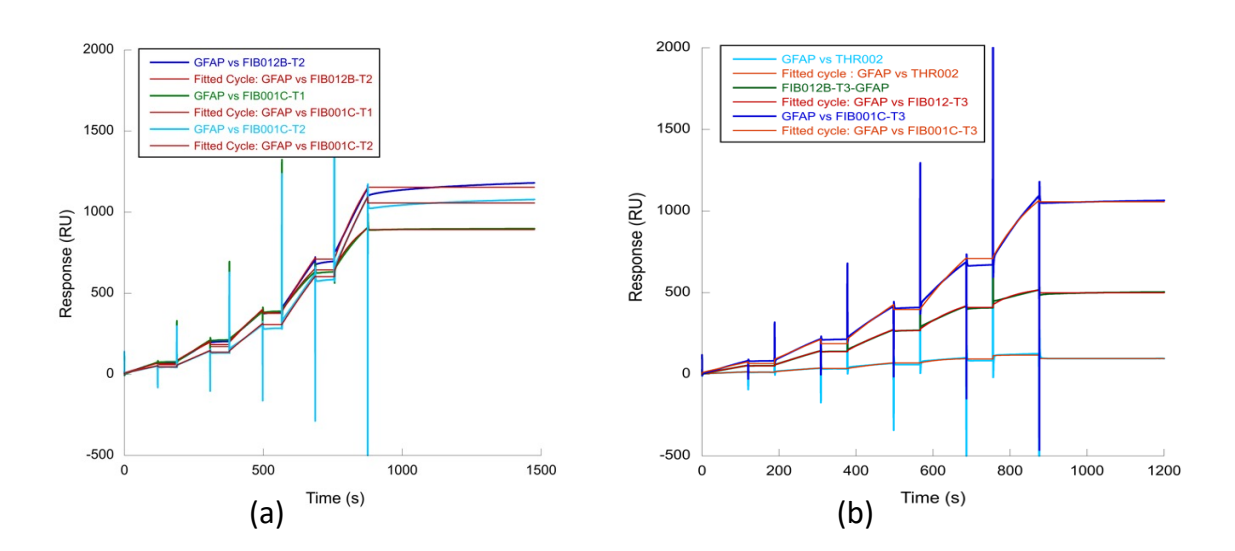


Figure 20: a) Single cycle kinetic analysis of the direct binding of FIBAC aptamer truncates to GFAP; b)

Single cycle kinetic analysis of the direct binding of FIBAC aptamer truncates to GFAP. Red curves indicate the 1:1 fitting model.

A thorough cross-reactivity study for the shortest variants of both aptamers (FIB001C-T3 and FIB012B-T3) was conducted where different control aptamers and control proteins were employed. The study used, a) two aptamers for two unrelated proteins, and b) testing GFAP truncated aptamers for binding with NF-L, which is also a co-biomarker in 2D-BioPAD.

Two unrelated aptamers AMI005B-T1 and HAVI1052C-T1 were immobilized on a streptavidin chip and 250nM GFAP was circulated over the chip. The results indicated no binding of GFAP with negative control aptamers (Figure 21a). In second experiment, NF-L protein was used as control target protein and 80 nM NF-L did not produce any binding signal when flown over immobilized FIB012B-T3, FIB001C-T3 and THR002 (a thrombin aptamer) aptamers (Figure 21b). These results confirmed the specificity of the GFAP aptamer truncates towards GFAP.



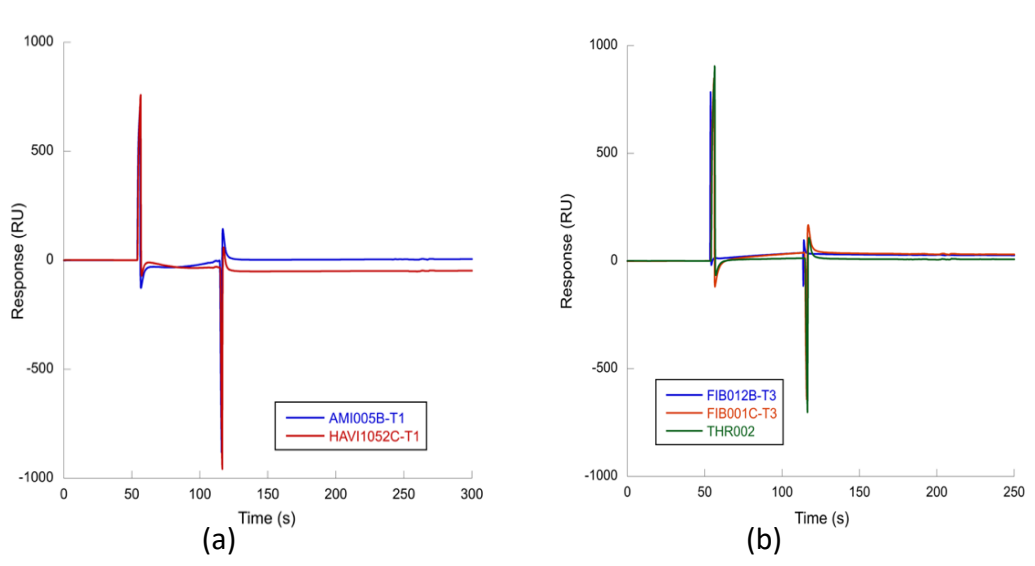


Figure 21: a) Sensorgrams following the injection of GFAP (250 nM) on control aptamers AMI005B-T1 and HAV1052C-T1; b) Sensorgrams following the injection of NFL (80 nM) on aptamers truncates FIB012B-T3, FIB001C-T3 and THR002 immobilized on the chip.

CeADAR assessed the binding scores of candidate aptamers with a higher interaction score generated through our pipeline, leveraging AptaMCTS recommendations for targets. The binding scores were computed using PDB files for Beta-amyloid peptide (1YT), pTau-217 (6X1), TBA with a partial of thrombin (1HUT), and GFAP (6A9P), with the implementation structure presented in Figure 15.

The results show a distinct variation in the binding scores for the candidate aptamers across different target proteins. As seen in Figures 22 and 23, the Beta-amyloid peptide shows the highest affinity, indicated by the steep and significant interaction curve, while the FIB001C – GFAP target displays relatively weaker interactions. These trends are reflected in the binding score distributions, where Beta-amyloid peptide achieves the highest overall binding scores, while GFAP show lower values compared with the baseline TBA model. The binding score values align with expected magnitudes, consistent with findings reported for similar other targets in the literature.<sup>38</sup>

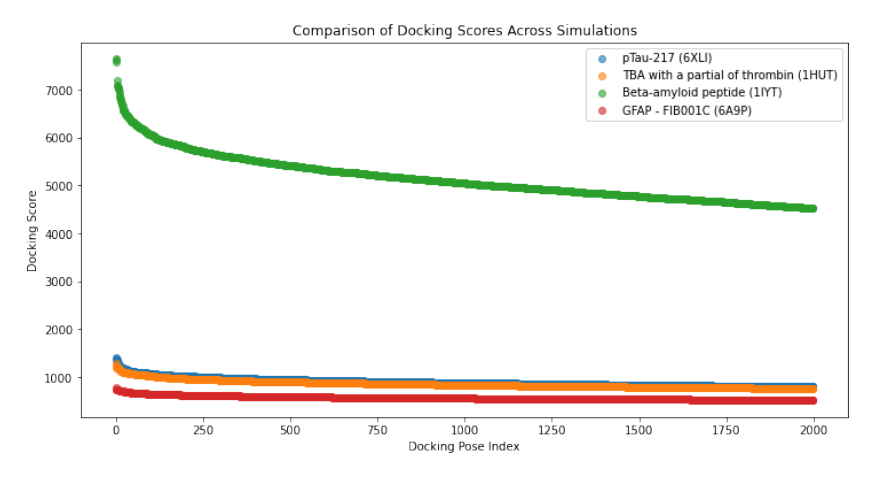


Figure 22: Binding score trends for AptaMCTS-Generated candidate aptamers – The interaction scores of candidate aptamers for Beta-amyloid peptide, pTau-217, TBA with a partial thrombin (1HUT), and FIB001C – GFAP targets, illustrating the variations in binding affinity across different pose index.



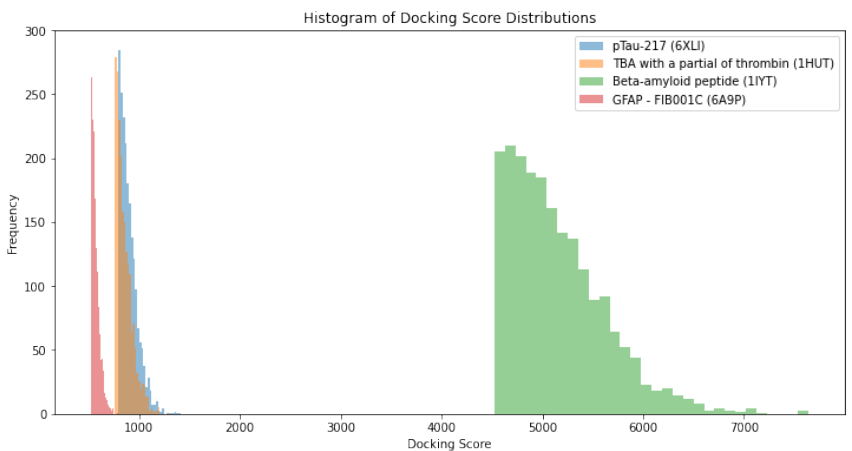


Figure 23. Binding score distribution across target proteins – Histogram representation of binding scores for each target, highlighting the distinct distribution patterns and the significantly higher scores observed for Beta-amyloid peptide.

The summary of the binding scores is provided in **Table 11**, where we report key statistics including mean scores, median scores, standard deviation, and thresholds for the top 5% of candidates. As shown, Beta-amyloid had the highest mean score of 5149.986, indicating a strong binding potential across multiple aptamers. In comparison, pTau-217 and GFAP exhibit lower mean scores, with pTau-217 at 902.972 and GFAP at 567.972, highlighting the challenges in achieving high-affinity binding with these targets. Additionally, the top 5% score threshold for Beta-amyloid is 6061.001, significantly higher than that of the other targets, suggesting its higher binding potential in the context of aptamer selection.

Table 11: Statistical summary of binding scores for candidate aptamers – Summary of mean, median, standard deviation, minimum, maximum scores, and top 5% score thresholds for aptamers targeting Beta-amyloid peptide, pTau-217, TBA with whole thrombin, and GFAP.

	Mean Score	Median Score	Standard Deviation	Minimum Score	Maximum Score	Top 5% Score Threshold
pTau-217 (6XLI)	902.972650	882.7200	86.926384	798.594	1410.447	1071.88270
TBA with a partial of thrombin (1HUT)	855.934088	834.1290	81.260515	760.840	1295.338	1021.71475
Beta-amyloid peptide (1IYT)	5149.986558	5049.2720	479.050430	4524.150	7642.179	6061.00055
GFAP - FIB001C (6A9P)	567.972173	556.8075	40.600747	520.136	795.256	647.64230

The binding score analysis shows that the candidate aptamers generated for Beta-amyloid peptide exhibit the highest binding efficiency, followed by pTau-217 and GFAP. The results suggest that the Beta-amyloid peptide target is the promising, while further optimization may be required for targets like GFAP to improve binding efficiency. The detailed statistical breakdown provides valuable insight into the distribution and performance of the aptamers for each target, providing direction for further computational advancements in aptamer selection.



# 4. Nanoparticles' Design & Synthesis

As part of WP2, **Aristotle University of Thessaloniki (AUTh)** is responsible for the design and synthesis of tailor-made magnetic nanoparticles (MNPs) to be conjugated with DNA aptamers. The goal is to create biphasic (Magnetite/Au) MNPs with controlled size, composition, and morphology, which will serve as platforms for enhanced biosensing. The gold component acts as a conjugation site for the selected DNA aptamers, while the magnetite core facilitates magnetic manipulation, enhancing sensitivity and enabling signal amplification.

AUTh investigated the physicochemical properties of the synthesized  $Fe_3O_4$ @Au nanoparticles and evaluated their magnetic and structural characteristics. The initial results showed promising magnetic performance and colloidal stability, but improvements were needed in terms of size control and aptamer conjugation efficiency. The insights gained guided the refinement of the synthesis process to produce nanoparticles with enhanced structural and functional properties.

### Synthesis of Core-Shell Fe<sub>3</sub>O<sub>4</sub>@Au Nanoparticles

In the previous phase of the project, AUTh examined different synthetic approaches targeting diverse nanoparticle morphologies, including:

- Decorated MNPs: Magnetite nanoparticles partially covered with gold clusters. The AuMNP conjugates were synthesized by the co-precipitation of Fe₃O₄ using phytic acid (IP6) as a solid template, facilitating the subsequent citrate reduction of Au nanoparticles. The Au NPs are embedded within the IP6-MNP matrix.
- Core—Shell Structures: Magnetite core coated with a uniform gold shell. Different variations
  of core—shell structures were examined. The most promising approach, which showed the
  best results for aptamer conjugation, involved enhancing long-term stability and size control
  over Au-SPIONs by using sodium citrate in the second stage of synthesis to further stabilize
  the particles, creating Cit-Au-SPIONs.
- **Janus MNPs:** Heterogeneous biphasic structures with magnetite and gold components forming asymmetrical dumbbell shapes.

Following a thorough evaluation of the structural, magnetic, and biosensing properties of these different morphologies, core-shell Fe<sub>3</sub>O<sub>4</sub>@Au nanoparticles emerged as the most promising platform. The core-shell configuration provided the best balance between magnetic manipulation, structural integrity, and efficient aptamer functionalization. Based on this outcome, we proceeded with the optimization and upscaling of the core-shell synthesis protocol.

#### **Synthesis Optimization**

The core size and shell thickness were regulated by adjusting key synthesis parameters, building on the optimization feedback from previous work. A modified method based on Stein et al. was developed at AUTh, introducing a simple aqueous synthesis for citrate-stabilized gold-coated SPIONs (Cit-Au-SPIONs) with enhanced size control and reproducibility. The optimization focused on refining citrate concentration and reaction pH to control reduction kinetics and gold nucleation, resulting in improved shell thickness and colloidal stability.

#### **Gold Shell Formation and Magnetic Separation**

The gold shell was deposited onto the magnetite core using citrate as a stabilizing and reducing agent. By optimizing the citrate concentration and reaction pH, the shell thickness and uniformity were significantly improved. Magnetic separation and washing steps were refined to minimize aggregation



and achieve a more uniform size distribution, enhancing the overall stability and performance of the nanoparticles.

Citrate concentration and pH were optimized to control shell thickness and uniformity while the final concentration of the core—shell MNPs samples was controlled to be around **0.15 to 0.20 mg/mL**.

#### **Synthetic modulations & corresponding features**

The synthesis conditions were systematically adjusted across different batches to evaluate the impact on the final nanoparticle properties with respect to MNPs concentration in the specimen (mg/mL):

- AuFe16: Higher magnetite content → MNPs ~1.03 mg/mL.
- AuFe17: Lower gold precursor input → MNPs ~0.06 mg/mL.
- AuFe18: Increased gold precursor input → MNPs ~0.16 mg/mL.
- AuFe19: Further increased gold precursor input → MNPs ~0.22 mg/mL.

These adjustments resulted in core sizes consistently below **30 nm** and well-defined gold shells, contributing to enhanced magnetic and biosensing performance.

**AuFe25** was synthesized as a repeat of **AuFe18**  $\rightarrow$  MNPs **~0.17 mg/mL** to assess reproducibility and validate the effectiveness of the synthetic protocol. Additionally, **AuFe24** was included as a reference gold nanoparticle sample, serving as a benchmark for comparison with previous reference samples.

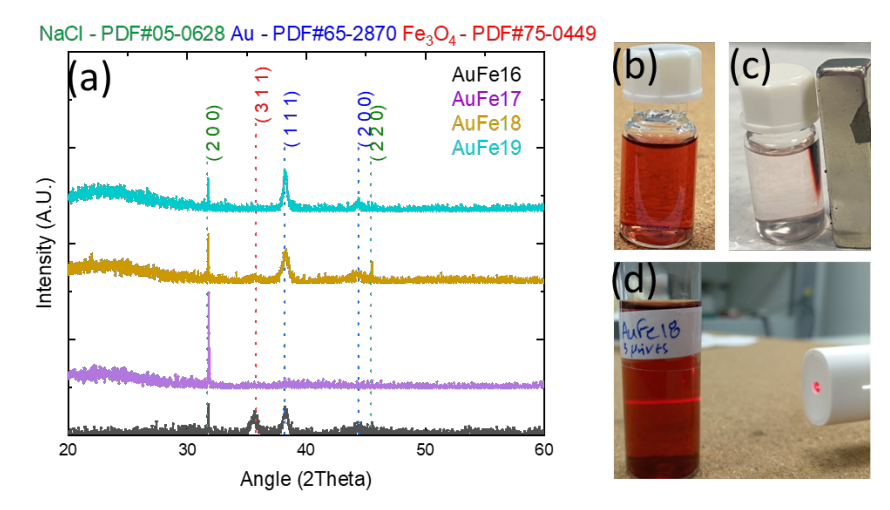


Figure 24: (a) X-ray Diffraction (XRD) pattern of the synthesized core—shell nanoparticles. (b) Core—shell sample AuFe18, showing a red wine color due to the gold shell. (c) The same sample after placing a magnet on the side for 3 days, attracting the MNPs and making the solution transparent. (d) Tyndall effect observed in a colloidal Au-Fe nanoparticle solution, indicating the presence of nanoscale particles through laser light scattering. The solution retained its stability after 3 months.

#### **Structural and Morphological Characterization**

Following the synthesis, the nanoparticles were structurally characterized using a combination of analytical techniques to validate the success of the refined synthesis protocol: **Crystallographic Structure:** XRD patterns (**Figure 24a**) displayed distinct diffraction peaks corresponding to both  $Fe_3O_4$  and Au phases, confirming the successful formation of biphasic core—shell structures. The sharpness of the peaks indicated high crystallinity of both components.

Hydrodynamic Size and Zeta Potential: Dynamic Light Scattering (DLS) was used to evaluate the size distribution and surface charge of the synthesized nanoparticles. DLS analysis (Figure 25a) indicated a mean hydrodynamic diameter of approximately 50 nm for the core—shell Fe<sub>3</sub>O<sub>4</sub>@Au nanoparticles:

Fe<sub>3</sub>O<sub>4</sub> core standalone = 20-30 nm

Core-shell Fe<sub>3</sub>O<sub>4</sub>@Au = ~30-50 nm



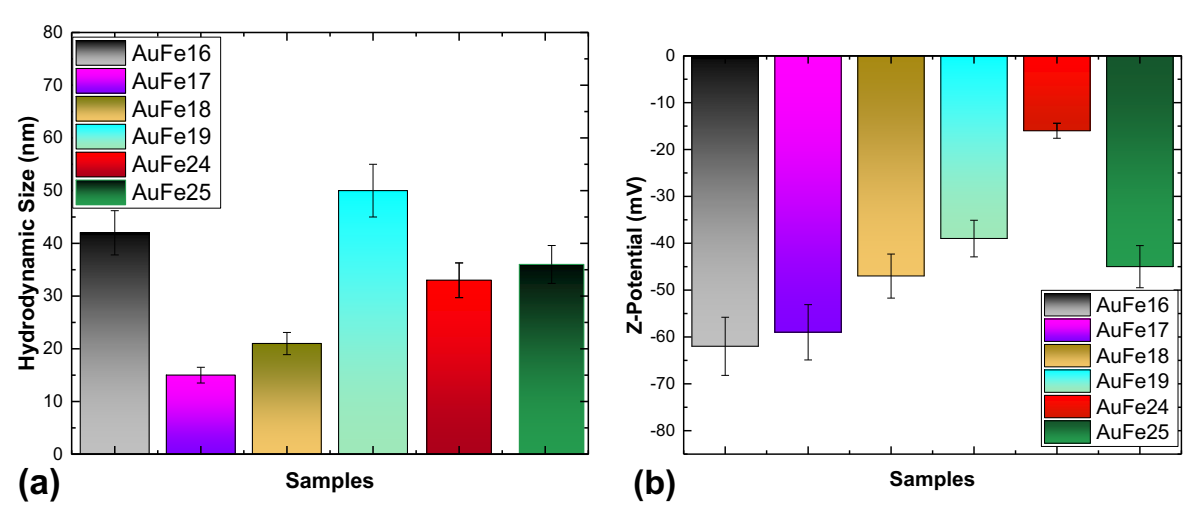


Figure 25: (a) Hydrodynamic size distribution of AuFe16, AuFe17, AuFe18, AuFe19, and AuFe15 core—shell Fe₃O₄@Au nanoparticles obtained from Dynamic Light Scattering (DLS), along with the reference gold nanoparticle sample AuFe24. (b) Zeta potential measurements of the core—shell nanoparticles, showing a surface charge between -40 and -60 mV, indicating high colloidal stability. The gold reference sample AuFe24 maintains a surface charge of -16 mV.

**Zeta Potential:** Zeta potential measurements (Figure 25b) confirmed a surface charge between -40 and -60 mV for  $Fe_3O_4$ @Au, suggesting high colloidal stability and strong electrostatic repulsion. The highly negative zeta potential enhances bio-interaction efficiency and reduces non-specific binding during bioassays.

**UV-Vis-NIR Absorption Spectra:** UV-vis-NIR absorption spectra were recorded to confirm the presence of gold in the core-shell Fe<sub>3</sub>O<sub>4</sub>@Au nanoparticles. Figure 26 shows the absorption spectra of AuFe16–19 MNPs samples, along with the reference Au nanoparticles sample AuFe24 and the reproducibility sample AuFe25. The characteristic plasmonic resonance of gold near 520-540 nm (indicated by the dotted line) is evident in all samples, confirming the successful formation of the gold shell. The sharper plasmonic peaks observed for AuFe18 and AuFe19 compared to AuFe16 and AuFe17 can be attributed to the increased gold content in these samples, leading to enhanced plasmonic activity. In contrast, the dense magnetite-rich sample AuFe16 exhibits a weaker plasmonic resonance due to the dominant contribution of magnetite, which Influences the overall optical response. The reference sample AuFe24 displays a well-defined plasmonic peak at 527 nm, validating the gold content and serving as a benchmark for comparison. The reproducibility sample AuFe25 shows a similar plasmonic profile to AuFe18, confirming the consistency and reliability of the synthetic protocol.



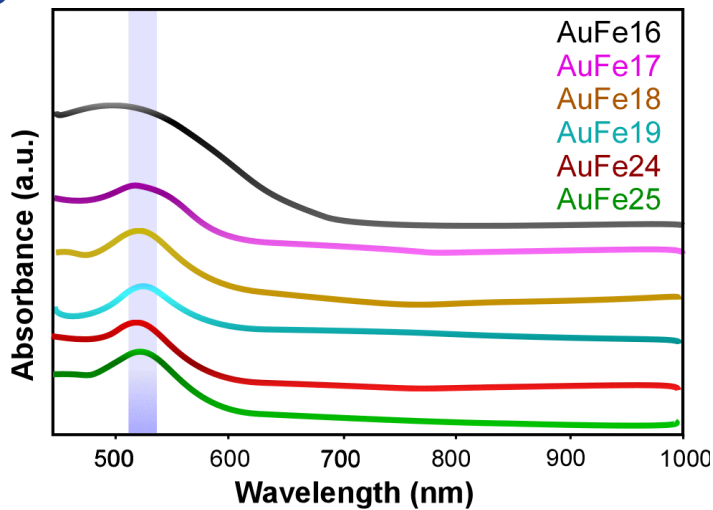


Figure 26: UV–vis–NIR absorption spectra of AuFe16, AuFe17, AuFe18, and AuFe19 core–shell Fe₃O₄@Au nanoparticles, along with the reference Au nanoparticles sample (AuFe24). The light blue transparent zone indicates the plasmonic resonance range of gold nanoparticles, typically between 520 nm for nanoparticles in the size range of 15–60 nm. The presence of a resonance within this zone in all samples confirms the successful formation of the gold shell. AuFe25, a reproducibility sample, exhibits a similar plasmonic profile to AuFe18, validating the consistency of the synthetic protocol.

The UV-vis-NIR absorption spectra between 500 nm and 600 nm were recorded for AuFe18 and AuFe18 conjugated with aptamers. Figure 27 shows that the plasmonic resonance of AuFe18 occurs at 525 nm, while upon conjugation with aptamers, the plasmonic resonance shifts slightly to 528 nm. This shift suggests successful conjugation of aptamers to the nanoparticle surface, indicating a change in the local environment around the gold nanoparticles due to the interaction with the biomolecules.

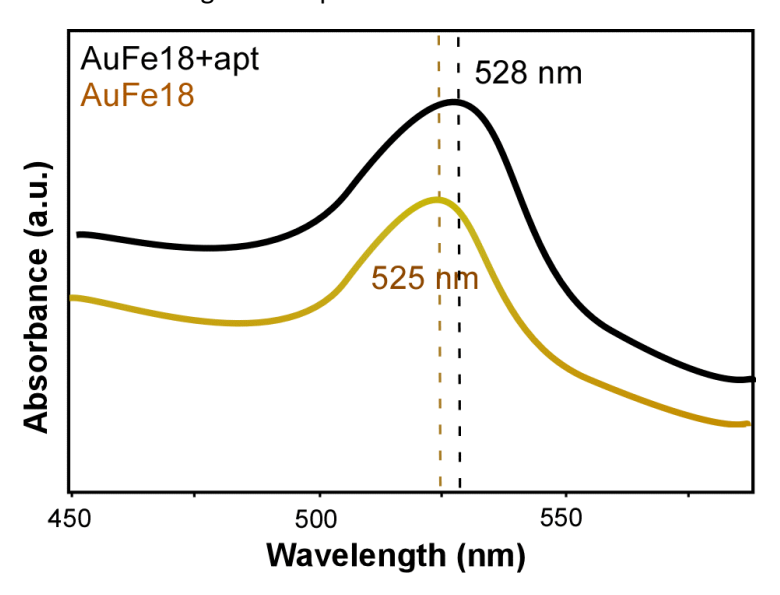


Figure 27: UV-vis-NIR absorption spectra between 450 nm and 600 nm of AuFe18 (yellow curve) and AuFe18 conjugated with aptamers (black curve). The plasmonic resonance of AuFe18 occurs at 525 nm, and upon conjugation with aptamers, the resonance shifts to 528 nm, indicating successful conjugation and a change in the local environment around the gold nanoparticles.

Dynamic Light Scattering (DLS) was used to evaluate the size distribution of AuFe18 before and after conjugation with aptamers. Figure 28a shows that the DLS size of AuFe18 is approximately 21 nm,



whereas after aptamer conjugation, the size increases to 66.4 nm. This significant size increase indicates successful conjugation of aptamers to the nanoparticle surface, leading to a larger hydrodynamic diameter due to the additional molecular layer around the nanoparticles.

Zeta potential measurements (Figure 28b) reveal a shift in surface charge from -47 mV (AuFe18 alone) to -37 mV (after aptamer conjugation), confirming the successful attachment of aptamers and the resulting modification of surface properties.

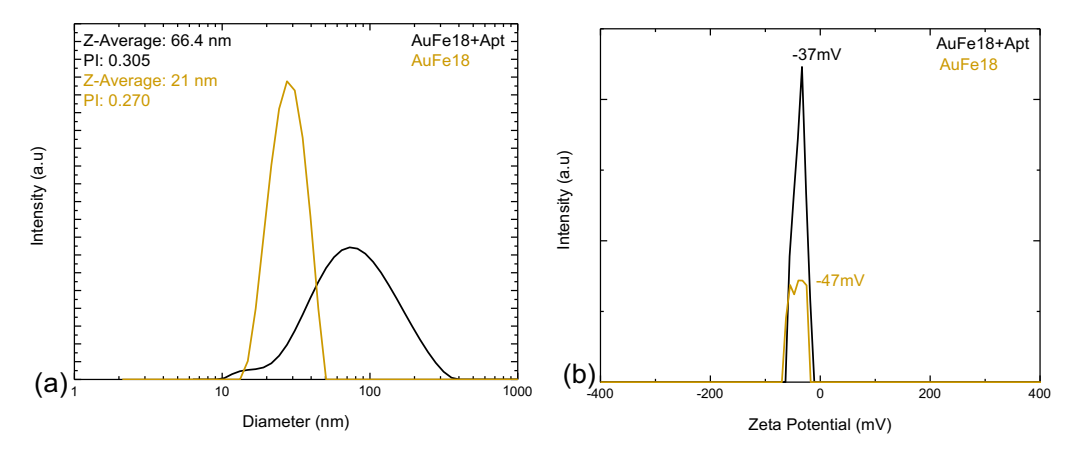


Figure 28: (a) DLS size distribution of AuFe18 before and after aptamer conjugation. The size of AuFe18 is measured at 21 nm, while the conjugation with aptamers results in an increased size of 66.4 nm, confirming successful aptamer binding and the formation of a larger hydrodynamic diameter. (b) Zeta potential measurements of AuFe18 before and after aptamer conjugation. The zeta potential shifts from -47 mV (AuFe18 alone) to -37 mV (after aptamer conjugation), indicating a decrease in surface charge due to the presence of aptamers on the nanoparticle surface.

#### **Optimization of MNPs**

What follows is the conjugation of  $Fe_3O_4$ @Au nanoparticles with DNA aptamers targeting Alzheimer's disease biomarkers. The conjugation process involved functionalizing the gold shell with thiolated aptamers via gold–thiol chemistry.

After evaluating the aptamer binding efficiency and biosensing performance, the core–shell  $Fe_3O_4$ @Au nanoparticles showed the most promising results in terms of signal sensitivity, specificity, and stability. This outcome guided the decision to further optimize the synthetic properties of the nanoparticles, aiming to improve:

- Core Size and Morphology: Further adjustments in the Fe<sup>2+</sup>/Fe<sup>3+</sup> ratio and reaction conditions were explored to fine-tune the size and shape of the magnetite core.
- **Gold Shell Thickness:** Modifications in citrate concentration and reaction temperature were introduced to precisely control the shell thickness and ensure uniform coverage.
- Magnetic Properties: The magnetite-to-gold ratio was systematically varied to balance enhanced magnetization with sufficient gold surface area for aptamer functionalization.

This optimization phase significantly improved the consistency and reproducibility of the core–shell nanoparticle synthesis, resulting in highly uniform  $Fe_3O_4$ @Au nanoparticles with tailored magnetic and structural properties.

The established synthetic protocol provides a robust platform for aptamer-based biosensing in Alzheimer's disease diagnostics. The next phase of the project will focus on further optimizing aptamer



conjugation and evaluating the biosensing performance of the Fe $_3O_4$ @Au nanoparticles in the detection of Alzheimer's disease biomarkers (A $\beta$ 40, A $\beta$ 42, p-Tau).

Next steps involve scaling up the synthesis of core—shell magnetite@Au nanoparticles and optimizing the bound aptamer content. The stability of both the magnetite@Au nanoparticles and the aptamer-conjugated nanoparticles will be improved under physiological conditions to ensure consistent performance. Additionally, the magnetization properties of the magnetic nanoparticle systems will be tuned to enhance their magnetic response to external fields, thereby improving target binding efficiency and overall assay performance. Conjugation experiments of RNV95 and A $\beta$ 7-92-1H1 amyloid peptides are under progress to validate a reliable detection platform. Surface plasmon resonance (SPR) measurements, together with dynamic light scattering (DLS) to determine the hydrodynamic size, will be routinely employed to assess the success of aptamer conjugation.



# 5. Conjugation of MNPs with Aptamers and

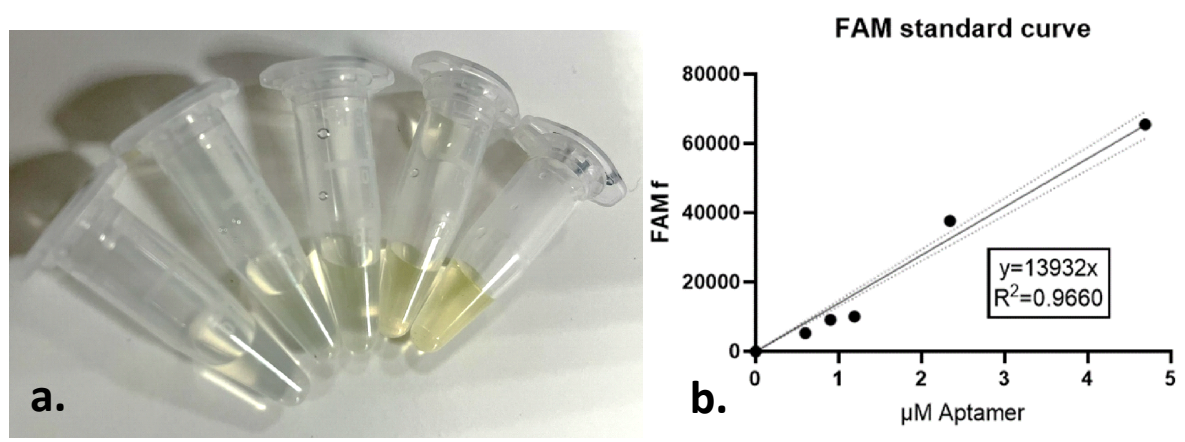
# Biomarkers The conjugation with

The conjugation with aptamers was achieved by using well-established cross-linking methodologies, aiming to (i) provide an adaptable and scalable solution that can easily be adjusted to different biomarkers; and (ii) target a 1 (MNP): 1 (aptamer) ratio to be achieved, further increasing the selectivity and specificity capability per biomarker. Conjugation of thiol-modified aptamers on gold magnetic nanoparticles (MNPs) was evaluated with the already established overnight freezing protocol<sup>51</sup>. To evaluate conjugation efficiency, FAM-modified fluorescent aptamers were employed. After conjugation, aptamers are detached from the MNPs and quantified with fluorometry. Furthermore, the conjugation of aptamers on MNPs was evaluated through the determination of electrophoretic mobility on agarose electrophoresis and the spectrophotometric analysis of the MNPs. Aptamer-modified MNPs' are expected to retain or even increase their absorbance, or present slight upshifts at their absorbance maxima. Moreover, the parameters of pH and dilution were evaluated to achieve higher concentrations of bound aptamer.

## **Conjugation Experimental Protocol**

### a. Conjugation of thiol-aptamer on MNPs

The conjugation phenomenon is extremely dependent on the type of the employed aptamer, the reaction pH, and temperature. To attach negatively charged DNA to negatively charged MNPs, a freezing-directed conjugation of DNA aptamers on nanoparticles was implemented, as it was proven adequate for various Au NPs, from 5 to 100 nm in diameter, and with several thiolated DNA sequences. In parallel with the already mentioned TBA1 aptamer, A $\beta$ 42 and A $\beta$ 40 aptamers were employed for conjugation in a series of MNPs. The A $\beta$ 42 aptamer that we chose to employ was the A $\beta$ -79-1H1 and for A $\beta$ 40 the RNV95. MNPs were mixed with SH-Aptamer of 0.2-5  $\mu$ M, at a final volume of 200  $\mu$ l, in sterile centrifuge tubes. <sup>53</sup>



\_

B. Liu and J. Liu Freezing Directed Construction of Bio/Nano Interfaces: Reagentless Conjugation, Denser Spherical Nucleic Acids, and Better Nanoflares, J. . Am. Chem. Soc. 139, 9471–9474 (2017).

Liu, B., Liu, J., Methods for preparing DNA-functionalized gold nanoparticles, a key reagent of bioanalytical chemistry. Anal. Methods 9, 2633-2643 (2017).

<sup>53</sup> See Appendix III for detailed conjugation protocol



Figure 29: (a) 6-Carboxyfluorescein (FAM)-modified thrombin aptamer solutions in Tris-EDTA (TE) buffer (From left to right: 0.6, 0.9, 1.19, 2.34, 4.69 μM). (b) Standard curve of the fluorescence of FAM-modified aptamers (Excitation 490 nm, emission 510-570 nm).

The tubes were kept at -20°C overnight and then thawed at room temperature and washed three times with 10mM tris-EDTA buffer (pH 8) to discard the unbound aptamers at 10,000 rpm, for 15 min, at 4°C. Finally, the aptamer-Au NPs were either stored in double distilled water (d.d.  $H_2O$ ), at 4°C, in the dark, or the bound aptamer was quantified after detachment, as described below.

#### b. Determination of bound aptamer

To detect and measure the amount of bound 6-Carboxyfluorescein (FAM)-modified aptamers on MNPs, the nano-conjugates were treated with 0.1 M DTT for 5 min at 50°C, followed by 1 h incubation at RT, in the dark. The immobilization of thiol-aptamer was optimized by monitoring the fluorescence intensities (Excitation: 490 nm, Emission: 510-570) of the bound FAM-labeled aptamer previously dissociated from the surface of nanoparticles (Figure 29a). The quantity of bound aptamer was determined with fluorescence (Excitation 490 nm, Emission 510-570 nm) at a Promega Glomax Multidetection system. The concentrations of the aptamers were evaluated using a fluorescence standard calibration curve for standard solutions of the thrombin aptamer (Figure 29b).

## c. Selection of magnetic carriers

The study aimed to evaluate the conjugation efficiency of thrombin-binding aptamer (TBA1) with MNPs of variable Au content: AuFe16(<0.05 mg/mL), AuFe17 (0.1 mg/mL), and AuFe18 (0.2 mg/mL). The goal was to determine which nanoparticle formulation exhibits the highest aptamer binding. A freeze-thaw method was employed overnight to facilitate aptamer binding to MNPs. The amount of bound aptamer was determined using FAM fluorescence detection at the blue spectrum. Quantification of bound aptamer revealed that AuFe18 (The one with the highest Au content 0.2 mg/mL) exhibited the highest conjugation efficiency as shown in fluorescence-based measurements (Figure 30).

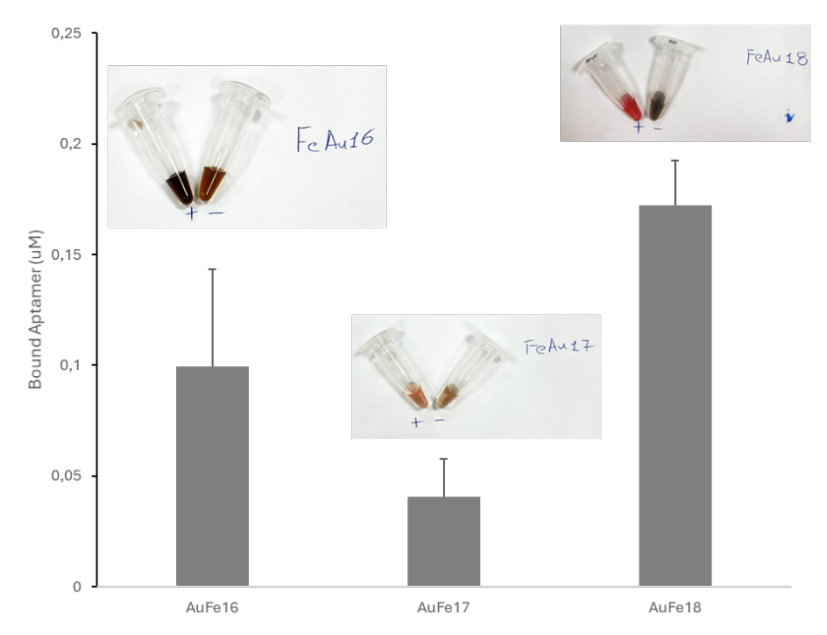


Figure 30: Conjugation efficiency of TBA1 aptamer with MNPs (AuFe16, AuFe17, AuFe18). The bar graph represents the amount of bound aptamer (in  $\mu$ M) detected via FAM fluorescence represented as Mean  $\pm$ 



Standard Deviation. Representative images of MNPs suspensions after conjugation are shown above each bar, demonstrating visual differences in nanoparticle behavior. The results indicate that AuFe18 exhibits the highest aptamer conjugation efficiency compared to AuFe16 and AuFe17.

The visual observation of nanoparticle suspensions also supported these findings, as demonstrated in the accompanying images. The study confirms that among the tested MNPs formulations, AuFe18 provides the highest degree of aptamer conjugation. This result suggests that AuFe18 is the most suitable candidate for further applications involving TBA1-functionalized nanoparticles.

#### d. Parameter tuning of conjugation: Dilution

To investigate the effect of dilution on the interaction between TBA1 and AuFe18 nanoparticles, we examined a 1/2 dilution as a potential Influencing parameter. Our results indicate that dilution did not facilitate a greater degree of thrombin aptamer binding (Figure 31). This outcome suggests that the binding efficiency is not solely dependent on nanoparticle concentration but may be influenced by other factors. Additionally, a lower nanoparticle concentration may have reduced the frequency of interactions between TBA1-conjugated AuFe18, thereby limiting binding opportunities. Moreover, dilution could have influenced the aggregation state of the nanoparticles, potentially altering the accessibility of aptamer binding sites. These findings suggest that while dilution affects the overall nanoparticle concentration, it does not necessarily enhance the aptamer-thrombin interaction under the conditions tested.

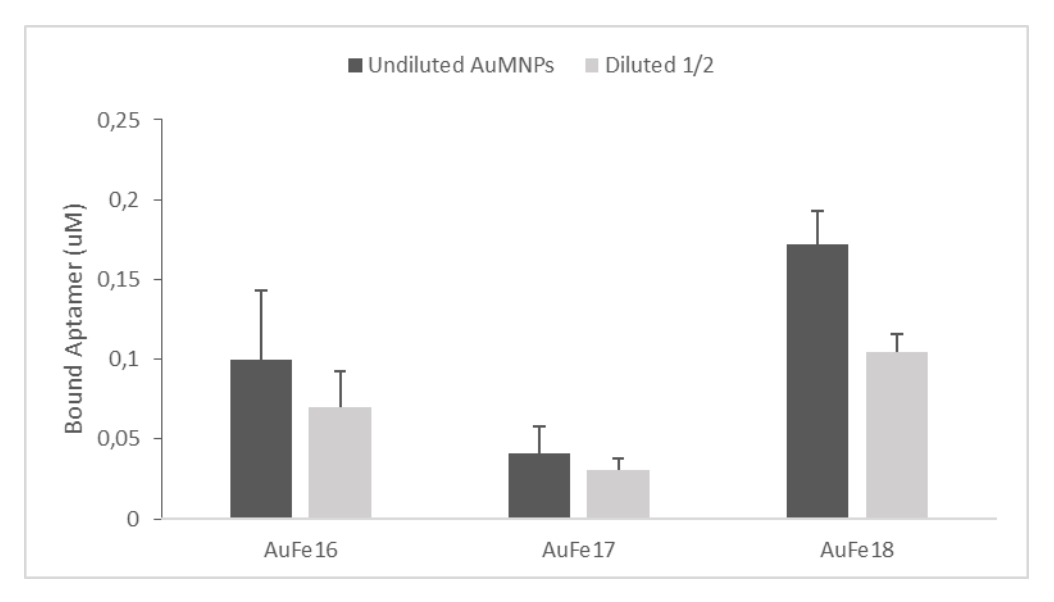


Figure 31: The bar graph represents the amount of bound aptamer (in µM) detected via FAM fluorescence represented as Mean ± Standard Deviation. The results indicate the dilution parameter has no effect on aptamer conjugation.



#### e. Parameter tuning of conjugation: pH environment

The interaction of TBA1 with AuFe18 was assessed at different pH levels (pH 3, 5, 7.4, and 8), along with a control in  $dH_2O$ . The results indicate that the conjugation efficiency is pH-dependent, with notable differences observed in the nanoparticle behavior under varying pH conditions.

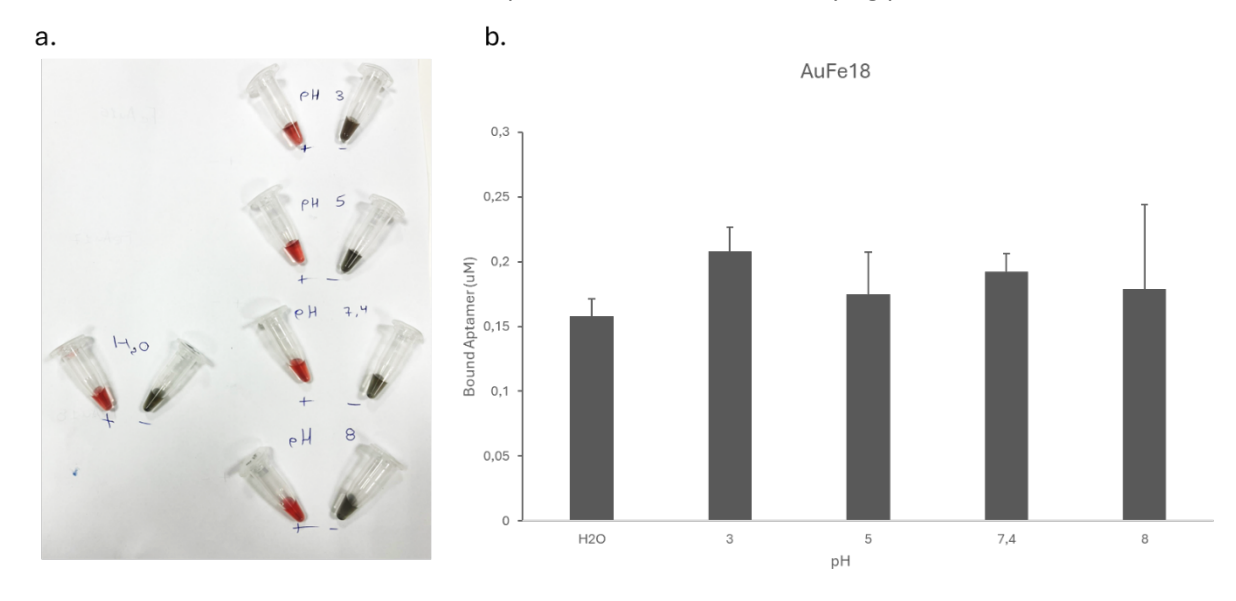


Figure 32: a. Effect of pH on the interaction between TBA1 and AuFe18 nanoparticles. The image shows nanoparticle suspensions at different pH levels (pH 3, 5, 7.4, and 8), along with a control in dH<sub>2</sub>O. The color variations and aggregation states indicate pH-independent changes in aptamer conjugation and nanoparticle stability. b. The bar graph represents the amount of bound aptamer (in μM) detected via FAM fluorescence represented as Mean ± Standard Deviation. The results indicate that in a buffer of pH= 3 the conjugation is higher without statistical significance.

The study confirms that among the tested Au MNPs formulations, AuFe18 provides the highest degree of aptamer conjugation. Additionally, pH was identified as a crucial parameter that has no significant interaction between the conjugation of TBA1 and AuFe18.

Future studies will explore the optimal pH conditions for stable and efficient aptamer functionalization (Figure 32). Further characterization of AuFe18, including stability and specificity studies across different pH conditions, will be conducted to validate its performance in relevant biological settings.

## f. Protocol application on amyloids

The conjugation of the mostly employed amyloid aptamers of the literature, namely RNV95 (targeting A $\beta$ 40) and A $\beta$ 7-H1-92 (targeting A $\beta$ 42), was studied with AuFe18, and the latest synthesized AuMNPs – AuFe25. Conjugation of aptamers on MNPs was performed with the overnight freezing protocol and the conjugated aptamer was detached and quantified with FAM fluorescence. The results for AuFe18 are provided in Figure 33 and for AuFe25 in Figure 34. Increasing the employed aptamer up to 2  $\mu$ M, for both RNV95 and A $\beta$ 7-H1-92, increased the

conjugated aptamer on both MNPs. However, a further increase of the concentration to 5  $\mu$ M led to either a drop or stabilization of conjugation efficiency. Conjugation efficiency was higher for AuFe18 in comparison with AuFe25. However, AuFe25 appeared to be more stable during the process, in all



aptamer concentrations, and surprisingly, it resisted aggregation even after overnight freezing, as seen in Figures 33c and 33d. Due to that, we proceeded to study further parameters with AuFe25.

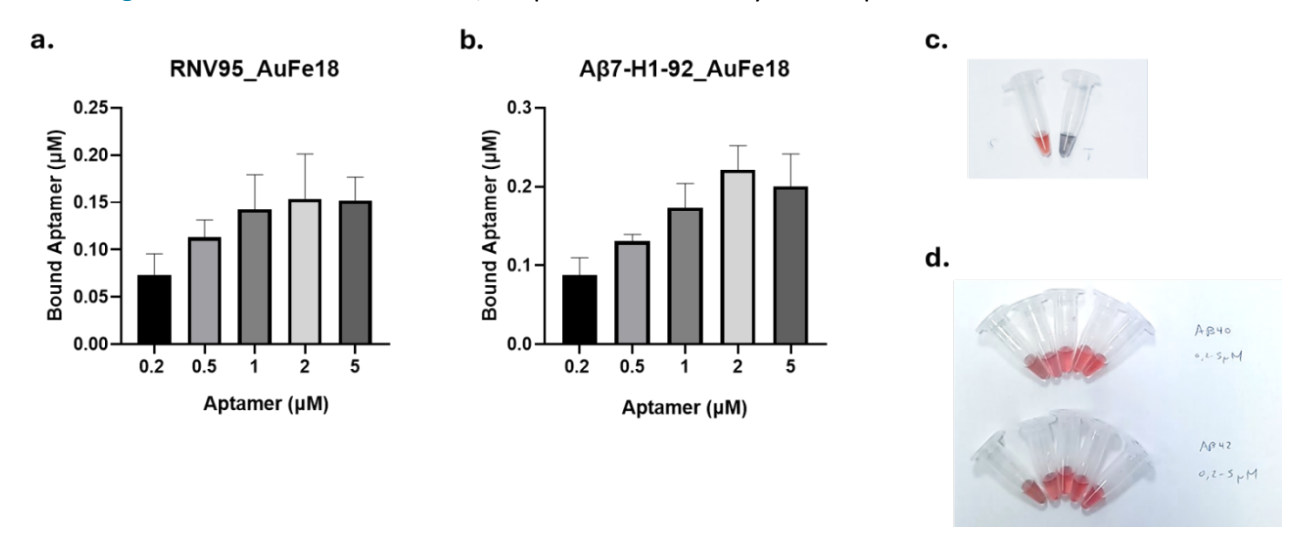


Figure 33: a. Conjugated RNV95 aptamer (A $\beta$ 40) and b. conjugated A $\beta$ -1H1-92 aptamer (A $\beta$ 42) aptamer on AuFe18 AuMNPs. The bar graph represents the amount of bound aptamer (in  $\mu$ M) detected via FAM fluorescence represented as Mean  $\pm$  Standard Deviation. c. AuFe18 AuMNPs after overnight freezing in the presence (left) or absence (right) of the aptamer. d. AuFe18 AuMNPs in the presence of 0.2-5  $\mu$ M of either RNV95 (top image) or A $\beta$ 7-H1-92 (bottom image) aptamers.

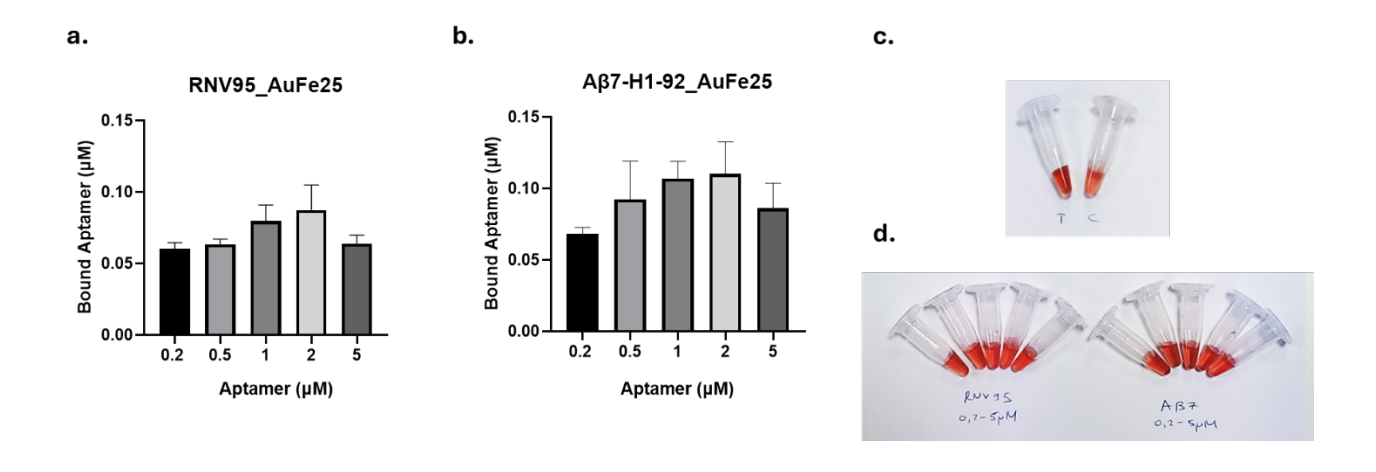


Figure 34: a. Conjugated RNV95 aptamer (Aβ40) and b. conjugated Aβ-1H1-92 aptamer (Aβ42) aptamer on AuFe25 MNPs. The bar graphs represent the amount of bound aptamer (in μM) detected via FAM fluorescence represented as MEAN ± Standard Deviation. c. AuFe25 MNPs after overnight freezing in the presence (left) or absence (right) of the aptamer. d. AuFe25 MNPs in the presence of 0.2-5 μM of either RNV95 (left) or Aβ7-H1-92 (right) aptamers.

#### g. Parameter tuning of conjugation of aptamers against amyloids on MNPs: pH effect

To study the effect of different buffers (pH and type of buffer chemicals) at conjugation efficiency on MNPs, we mixed AuFe25 with 1  $\mu$ M of either RNV95 or A $\beta$ -7-H1-92 aptamers and after 15 min, we added the following buffers at a final concentration of 10 mM: i) citrate-Na<sub>3</sub> (pH 3), ii) carbonate (pH



5), iii) HEPES-Na (pH 7.6), iv) Tris-EDTA (pH 8). The samples were then treated as previously described and the amount of the conjugated aptamers on MNPs was quantified.

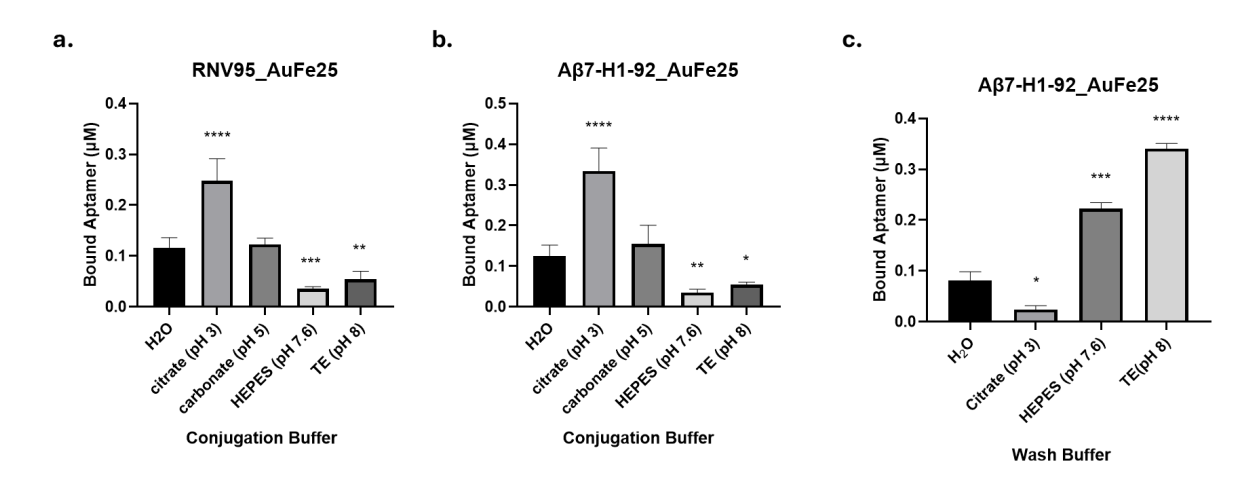


Figure 35: a, b. The effect of different pH/buffers during the conjugation of 1  $\mu$ M of either RNV95 aptamer (A $\beta$ 40) or A $\beta$ 7-92-1H1 aptamer (A $\beta$ 42) on AuFe25 AuMNPs. c. The effect of different pH/buffers during the wash of A $\beta$ 7-H1-92-functionalized AuFe25. The bar graphs represent the amount of bound aptamer (in  $\mu$ M) detected via FAM fluorescence represented as Mean  $\pm$  Standard Deviation. Analysis was performed with one-way ANOVA (Dunnet's correction).

As presented in Figures 35a and 35b, if conjugation is performed at pH 3, a significant increase in conjugation efficiency for both RNV95 and Aβ7-H1-92 aptamers was documented, while a significant drop of efficiency was determined for pH values above 7.6. This effect was previously documented for AuNPs, with low pH values providing better attachment of the thiolated aptamers on Au, supposedly attributed to stabilization of carboxyl groups' charge of the citrate capped NPs.<sup>54</sup> Interestingly, as seen in Figure 35c, the highest aptamer-MNPs stability was found with washes employing TE buffer, while citrate buffer washes destabilized aptamer-MNPs nanoconjugates. Thus, it was decided to proceed with pH 3-buffer addition after mixing aptamers with MNPs during overnight freezing conjugation, while the following washes will be performed with TE buffer.

## h. Parameter tuning of conjugation on amyloids: Salt addition

To study the possible effect of ionic strength during conjugation, an addition of 30-300 mM of NaCl was performed after mixing A $\beta$ 7-H1-92 aptamer with AuFe25 and citrate buffer, pH 3. After adding citrate buffer, samples were incubated for a further 15 min and conjugation efficiency was determined after overnight freezing.

As depicted in Figure 36, no statistically significant increase in conjugation efficiency was documented. On the other hand, the addition of high salt concentrations (150 or 300 mM) significantly decreased the conjugation efficiency. It is hypothesized that high salinity leads to unstable MNPs' dispersity during conjugation, impeding the linking of aptamers on Au. Consequently, we chose not to add further NaCl during conjugation.

<sup>&</sup>lt;sup>54</sup> Zhang et al. <u>Surface Science of DNA Adsorption onto Citrate-Capped Gold Nanoparticles</u>, Langmuir 28/8 (2012).



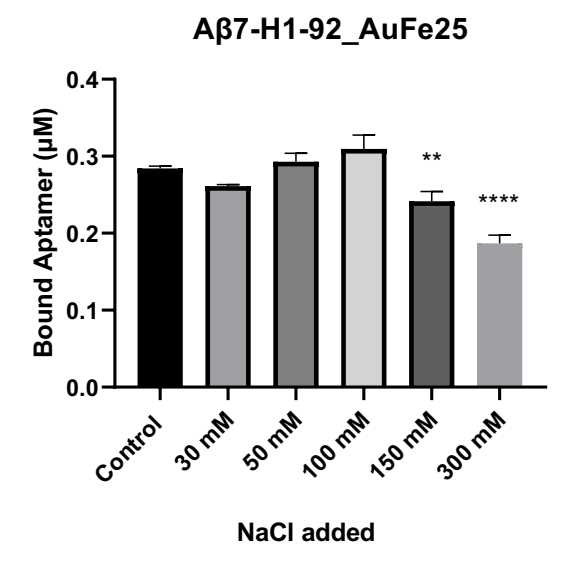


Figure 36: The effect of different NaCl concentrations during the conjugation of 1  $\mu$ M of A $\beta$ 7-1H1-92 aptamer (A $\beta$ 40) on AuFe25 MNPs. The bar graphs represent the amount of bound aptamer (in  $\mu$ M) detected via FAM fluorescence represented as Mean  $\pm$  Standard Deviation. Analysis was performed with one-way ANOVA (Dunnet's correction).

The latest studies based on TBA1, RNV95 and A $\beta$ 7-1H1-92 aptamers have provided significant information on a successful conjugation protocol for MNPs. Conjugation of thiol-modified aptamers is greatly enhanced when using acidic conditions, and specifically in the presence of 10 mM citrate-Na buffer, pH 3. The conjugation is performed overnight in freezing conditions, without the addition of further salt. Following that, MNP-aptamer conjugates are washed with TE buffer, pH 8 and resuspended in TE. Some following factors to be studied is the possible increase in conjugation efficiency with more concentrated MNP suspensions, the addition of salts to TE buffer for washes and/or storage of nanoparticles. Studies with the suggested aptamer for GFAP by Novaptech (FIB001C/T3) will also begin to verify the universality of the standardized protocol.

Furthermore, studies are now in the process for the ability of these nanoconjugates to successfully bind their target peptides. Pre-experiments with SDS-PAGE electrophoresis suggest binding of MNP-TBA1 conjugates with thrombin (as presented in the D2.1 deliverable). Currently we are working with a specific antibody against thrombin protein to implement Western blotting and ELISA analysis on proving the binding with the target peptide. In addition, we have ordered A $\beta$  peptides to test the nanoconjugates with the corresponding A $\beta$  aptamers.



# 6. Next Steps & Critical Milestones

The activities conducted under WP2 of the 2D-BioPAD project, focusing on the identification, synthesis, and evaluation of aptamers for AD protein biomarkers and the synthesis and characterization of MNPs as carriers, have made significant progress. We have made strides in the identification of DNA aptamers specific to key AD biomarkers, including A $\beta$ 40, A $\beta$ 42, NFL, GFAP, and p-tau 217. This task is still ongoing, with further work required to finalize the selection of aptamers for these protein biomarkers.

Key Performance Indicator 1 corresponds to Protein Biomarkers for early AD diagnosis, and it is expected to be concluded at M24. Accordingly, Key Performance Indication 30 corresponds to identification of 5 DNA aptamers per target and evaluation for their binding properties and specificity. Progress towards these KPIs and corresponding milestones are as follows:

Al: We have narrowed down how to translate the indicative aptamers to contribute to a better experimental development, following literature model metrics. Using AptaTrans, we are currently evaluating protein sequences to identify promising aptamer candidates with good interaction scores. This includes TBA as a baseline modelling and conducting a detailed analysis of GFAP and NFL sides. Further collaboration with partners such as NOVA and ICN2 have been agreed, looking for the design of aptamers that follow their experimental requirements as shown in their tasks, and addressing the setbacks that are presented experimentally with target biomarkers such as Beta amyloid (A $\beta$ ), where their complex behaviour causes problems binding the aptamers. (18th-24<sup>th</sup> month).

**NFL:** The full-length aptamers identified for Nfl will be truncated. To limit the cross-reactivity of the currently identified aptamers, truncation approach will be decided on selective and sequential removal of sequence portions. The expected outcome is retaining the elements responsible for recognizing Nfl only, and, hence providing a better specificity. Besides this, the other ongoing selections at characterization phases are also expected to yield more aptamers. Further, the currently running selections will be modified with negative selection approaches to minimize cross reactivity. (18<sup>th</sup>-30<sup>th</sup> month).

**GFAP:** High affinity aptamers have been selected against GFAP and truncation of these aptamers has generated short and specific GFAP aptamers. These aptamers are now being conjugated to nanoparticles for signal amplification in graphene sensor. Conducting preliminary experiments on the conjugation of the FIB001C/T3 aptamer and its interaction with the GFAP protein are next steps in the process. Positive results from new aptamer selections are also expected to give more aptamers for GFAP.(18<sup>th</sup>-24<sup>th</sup> month).

**Aß40 and Aß42:** We are currently examining the conjugation of commercially available aptamers: for Aβ40, RNV95<sup>55</sup> (previously described as suitable aptamer for use in a wide range of affinity assays to detect low-molecular-weight Aβ40 oligomers)<sup>56</sup> and Aβ7-92-1H1<sup>57</sup> (previously described to possess high specificity for the Aβ42 monomer).<sup>58</sup> Conjugation efficiency of these aptamers with the

-

<sup>&</sup>lt;sup>55</sup> 5'-TGGGGGGCGACGATAGGGGCCCCCGGTAGGATGGACG-3'

<sup>&</sup>lt;sup>56</sup> Chakravarthy M et al. <u>Development of DNA aptamers targeting low-molecular-weight amyloid-β peptide aggregates: In vitro</u> Chem Commun 54:4593–4596 (2018).

<sup>&</sup>lt;sup>57</sup> 5'-CCGGTGGGGACCAGTACAAAAGTGGGTAGGGCGGGTTGGAAAA-3

<sup>&</sup>lt;sup>58</sup> Zheng Yet al., <u>Development of DNA Aptamer as a β-Amyloid Aggregation Inhibitor</u>. ACS Appl Bio Mater. 3, 12, 8611–8618 (2020).



synthesized MNPs and amyloid peptides will be evaluated with the involvement of sophisticated immunological techniques (Western blotting, commercial ELISA kits, Dot blotting) in combination with specific antibodies for amyloid peptides  $\beta$ -Amyloid (1-42) (D9A3A) Rabbit mAb #14974 and  $\beta$ -Amyloid (1-40) (D8Q7I) Rabbit mAb Cell Signaling Technology). Conjugating RNV95 and A $\beta$ 7-92-1H1 with AuNPs. A $\beta$  peptides have been ordered to evaluate the binding efficiency of aptamers to their target peptides. (18<sup>th</sup>-30<sup>th</sup> month).

**pTau217** has commercial availability issues. Hence in a workaround, the aptamer selection is currently undergoing against small peptides covering the region of interest on protein. Once the selection is completed, the candidates obtained will be tested rigorously for binding with pTau-217 protein. Specific antibodies for Tau (D1M9X) XP Rabbit mAb (46687, Cell Signaling Technology) and for Phospho-Tau (Thr231) (#71429, Cell Signaling Technology), are under study to evaluate alternative binding options. (18<sup>th</sup>-30<sup>th</sup> month).

MNPs: core-shell Fe $_3O_4$ /Au magnetic nanoparticles are routinely synthesized and conjugated with validated protocol with corresponding aptamers. So far TBA and A $\beta$ 40 and A $\beta$ 42 are effectively conjugated with MNPs. All specimens, once effectively conjugation of MNPs with aptamers is achieved, are progressing in examining binding efficiency with biomarkers. Such samples are handed to consortium partners to integrate them in the subsequent steps of sensor manufacture i.e. graphene-based sensing platform. This upcoming work is essential for developing standardized nanobased probes aimed at early AD diagnosis and may require further functionalization steps according to biomarker specific MNPs/aptamers integration to the sensing platform (18<sup>th</sup>-30<sup>th</sup> month).

Accordingly, the status of the 4 objectives of WP2: Biomarkers binding and quantitative analysis are as follows:

Objective	Description	Status
2.1	Identification, synthesis, functionalization, and optimization of DNA aptamers for AD protein biomarkers.	Ongoing for 5 Biomarkers.
2.2	Identification, synthesis, characterization, and evaluation of MNPs as carriers and enablers.	Completed. Further optimization steps may arise when integrating to platform (WP3).
2.3	Conjugation of aptamers, MNPs, and Biomarkers with AD protein biomarkers.	Underway for A $\beta$ 40 and A $\beta$ 42 and GFAP. Wait for aptamer selection for pTau and NFL.
2.4	Evaluation and validation of individual and conjugated components.	Ongoing for all conjugation cases: MNPs/Aptamers, MNPs/Aptamers/Biomarkers

Overall, WP2 is on track, with key milestones being met. Continued efforts in aptamer conjugation with biomarkers will be crucial for the successful achievement of WP2 and for paving the way for subsequent work packages in the project.

-

<sup>&</sup>lt;sup>59</sup> This rabbit monoclonal antibody specifically recognizes the human Aβ42 isoform. The conjugation of Aβ7-92-1H1 to Aβ42 can be detected using Western Blot and/or ELISA methods with this antibody. This antibody will be used after the detachment of Aβ42 peptide from its corresponding aptamer, in order to prove that RNV95 binds specifically the Aβ40 peptide.



# Amyloid beta and monomerization protocol

Amyloid beta is highly prone to form aggregates and thus the preparation of a sample free of aggregates is challenging. There are several methods claiming to produce an aggregate-free sample from lyophilized amyloid peptide, such as pre-treatment with sodium hydroxide (NaOH), ammonium hydroxide (NH4OH) or 1,1,1,3,3,3-Hexafluoroisopropanol (HFIP) and resuspension in NaOH, dimethylsulfoxide (DMSO), phosphate-buffered saline (PBS), HEPES buffer or water. Among these methods, the most commonly used is the pre-treatment with HFIP<sup>60</sup>.

#### HFIP Treatment<sup>61</sup>

- 1. Dissolve the lyophilized A $\beta$  peptide in 100% HFIP to a concentration of 1 mg/mL.
- 2. Vortex gently to ensure complete dissolution.
- 3. Incubate the solution at room temperature for 1 hour to ensure thorough disaggregation.
- 4. Evaporate HFIP ideally with SpeedVac without heating to lyophilize the peptide into a thin film. Alternatively, lyophilize under a gentle stream of nitrogen or argon gas.<sup>62</sup>
- 5. The HFIP treated amyloid beta lyophilized samples were stored at -20 °C until use.

### Aß dissolution

- 1. Prior to resuspension, each vial was allowed to reach room temperature (~30 min) and was centrifuged (3,000 g at RT for 1 min) to ensure maximal peptide recovery.
- 2. The peptide was then dissolved in 10 mM NaOH to a concentration of 1 mg/mL peptide injected into the vial using a syringe. Alternatively, 100% anhydrous DMSO can also be employed.<sup>63</sup>
- 3. Each vial is vortexed gently for 30-60 seconds to ensure that all peptides will be dissolved in the solution added without  $A\beta$  fibrils to be formed. Some sonication for up to 5 minutes may also help in the process.
- 4. The final concentration should be finally determined with a spectrophotometric assay (i.e. BCA assay kit, nanodrop etc).

#### Aβ storage

- 1. Aliquoting prevents repeated freeze-thaw cycles, which can induce aggregation.
- 2. Divide the peptide solution into single-use aliquots **in low-binding**, polypropylene microcentrifuge tubes (e.g., 50 µL per tube).
- 3. Flash-freeze the aliquots in liquid nitrogen or a dry ice/ethanol bath.
- 4. Store at -80°C until use.
- 5. Avoid repeated freeze-thaw cycles, as they can promote aggregation. Aliquots concentration may also vary due to amyloid sticking to the tube. Final concentration should be determined again.

#### **Aβ** solutions for Experimental Use

- 1. Thaw an aliquot rapidly at 37°C.
- 2. Immediately dilute and gently mix with the pre-warmed assay buffer (e.g., PBS, HEPES) to achieve the final working concentration.

\_

<sup>&</sup>lt;sup>60</sup> Taylor, A. I. P., et al., <u>Simple, Reliable Protocol for High-Yield Solubilization of Seedless Amyloid-β Monomer</u>. ACS chemical neuroscience, 14(1), 53–71 (2023).

<sup>&</sup>lt;sup>61</sup> While HFIP effectively monomerizes Aβ, residual HFIP must be removed to prevent interference with subsequent steps

<sup>&</sup>lt;sup>62</sup> Ensure complete removal of HFIP to prevent residual solvent from affecting peptide behavior. Critical point: Ensure by measuring again the concentration

 $<sup>^{63}</sup>$  DMSO is effective in maintaining A $\beta$  in a monomeric state, reducing the likelihood of aggregation during handling



# pTau-217 sequence under study

"...VAVVRTPPKSPSSAKSRLQTAPVPMPDLKNVKSKIGSTENLKHQPGGGKVQIINKKLDLSNVQSKCGSKDNIKHVPGGGSV QIVYKPVDLSKVTSKCGSLGNIHHKPGGGSVQIVYKPVDLSKVTSKCGSLGNIHHKPGGGSVQIVYKPVDLSKVTSKCGSLGNIH HKPGGGSVQIVYKPVDLSKVTSKCGSLGNIHHKPGGGSVQIVYKPVDLSKVTSKCGSLGNIHHKPGGGSVQIVYKPVDLSKVTSK CGSLGNIHHKPGGGSVQIVYKPVDLSKVTSKCGSLGNIHHKPGGGSVQIVYKPVDLSKVTSKCGSLGNIHHKPGGGSVQIVYKP VDLSKVTSKCGSLGNIHHKPGGGSVQIVYKPVDLSKVTSKCGSLGNIHHKPGGGSVQIVYKPVDLSKVTSKCGSLGNIHHKPGG GSVQIVYKPVDLSKVTSKCGSLGNIHHKPGGGSVQIVYKPVDLSKVTSKCGSLGNIHHKPGGGSVQIVYKPVDLSKVTSKCGSLG NIHHKPGGGSVQIVYKPVDLSKVTSKCGSLGNIHHKPGGGSVQIVYKPVDLSKVTSKCGSLGNIHHKPGGGSVQIVYKPVDLSKV TSKCGSLGNIHHKPGGGSVQIVYKPVDLSKVTSKCGSLGNIHHKPGGGSVQIVYKPVDLSKVTSKCGSLGNIHHKPGGGSVQIVY KPVDLSKVTSKCGSLGNIHHKPGGGSVQIVYKPVDLSKVTSKCGSLGNIHHKPGGGSVQIVYKPVDLSKVTSKCGSLGNIHHKPG GGSVQIVYKPVDLSKVTSKCGSLGNIHHKPGGGSVQIVYKPVDLSKVTSKCGSLGNIHHKPGGGSVQIVYKPVDLSKVTSKCGSL GNIHHKPGGGSVQIVYKPVDLSKVTSKCGSLGNIHHKPGGGSVQIVYKPVDLSKVTSKCGSLGNIHHKPGGGSVQIVYKPVDLS KVTSKCGSLGNIHHKPGGGSVQIVYKPVDLSKVTSKCGSLGNIHHKPGGGSVQIVYKPVDLSKVTSKCGSLGNIHHKPGGGSVQI VYKPVDLSKVTSKCGSLGNIHHKPGGGSVQIVYKPVDLSKVTSKCGSLGNIHHKPGGGSVQIVYKPVDLSKVTSKCGSLGNIHHK PGGGSVQIVYKPVDLSKVTSKCGSLGNIHHKPGGGSVQIVYKPVDLSKVTSKCGSLGNIHHKPGGGSVQIVYKPVDLSKVTSKCG SLGNIHHKPGGGSVQIVYKPVDLSKVTSKCGSLGNIHHKPGGGSVQIVYKPVDLSKVTSKCGSLGNIHHKPGGGSVQIVYKPVDL SKVTSKCGSLGNIHHKPGGGSVQIVYKPVDLSKVTSKCGSLGNIHHKPGGGSVQIVYKPVDLSKVTSKCGSLGNIHHKPGGGSV QIVYKPVDLSKVTSKCGSLGNIHHKPGGGSVQIVYKPVDLSKVTSKCGSLGNIHHKPGGGSVQIVYKPVDLSKVTSKCGSLGNIH HKPGGGSVQIVYKPVDLSKVTSKCGSLGNIHHKPGGGSVQIVYKPVDLSKVTSKCGSLGNIHHKPGGGSVQIVYKPVDLSKVTSK CGSLGNIHHKPGGGSVQIVYKPVDLSKVTSKCGSLGNIHHKPGGGSVQIVYKPVDLSKVTSKCGSLGNIHHKPGGGSVQIVYKP VDLSKVTSKCGSLGNIHHKPGGGSVQIVYKPVDLSKVTSKCGSLGNIHHKPGGGSVQIVYKPVDLSKVTSKCGSLGNIHHKPGG GSVQIVYKPVDLSKVTSKCGSLGNIHHKPGGGSVQIVYKPVDLSKVTSKCGSLGNIHHKPGGGSVQIVYKPVDLSKVTSKCGSLG NIHHKPGGGSVQIVYKPVDLSKVTSKCGSLGNIHHKPGGGSVQIVYKPVDLSKVTSKCGSLGNIHHKPGGGSVQIVYKPVDLSKV TSKCGSLGNIHHKPGGGSVQIVYKPVDLSKVTSKCGSLGNIHHKPGGGSVQIVYKPVDLSKVTSKCGSLGNIHHKPGGGSVQIVY KPVDLSKVTSKCGSLGNIHHKPGGGSVQIVYKPVDLSKVTSKCGSLGNIHHKPGGGSVQIVYKPVDLSKVTSKCGSLGNIHHKPG GGSVQIVYKPVDLSKVTSKCGSLGNIHHKPGGGSVQIVYKPVDLSKVTSKCGSLGNIHHKPGGGSVQIVYKPVDLSKVTSKCGSL GNIHHKPGGGSVQIVYKPVDLSKVTSKCGSLGNIHHKPGGGSVQIVYKPVDLSKVTSKCGSLGNIHHKPGGGSVQIVYKPVDLS KVTSKCGSLGNIHHKPGGGSVQIVYKPVDLSKVTSKCGSLGNIHHKPGGGSVQIVYKPVDLSKVTSKCGSLGNIHHKPGGGSVQI VYKPVDLSKVTSKCGSLGNIHHKPGGGSVQIVYKPVDLSKVTSKCGSLGNIHHKPGGGSVQIVYKPVDLSKVTSKCGSLGNIHHK PGGGSVQIVYKPVDLSKVTSKCGSLGNIHHKPGGGSVQIVYKPVDLSKVTSKCGSLGNIHHKPGGGSVQIVYKPVDLSKVTSKCG SLGNIHHKPGGGSVQIVYKPVDLSKVTSKCGSLGNIHHKPGGGSVQIVYKPVDLSKVTSKCGSLGNIHHKPGGGSVQIVYKPVDL SKVTSKCGSLGNIHHKPGGGSVQIVYKPVDLSKVTSKCGSLGNIHHKPGGGSVQIVYKPVDLSKVTSKCGSLGNIHHKPGGGSV QIVYKPVDLSKVTSKCGSLGNIHHKPGGGSVQIVYKPVDLSKVTSKCGSLGNIHHKPGGGSVQIVYKPVDLSKVTSKCGSLGNIH HKPGGGSVQIVYKPVDLSKVTSKCGSLGNIHHKPGGGSVQIVYKPVDLSKVTSKCGSLGNIHHKPGGGSVQIVYKPVDLSKVTSK CGSLGNIHHKPGGGSVQIVYKPVDLSKVTSKCGSLGNIHHKPGGGSVQIVYKPVDLSKVTSKCGSLGNIHHKPGGGSVQIVYKP VDLSKVTSKCGSLGNIHHKPGGGSVQIVYKPVDLSKVTSKCGSLGNIHHKPGGGSVQIVYKPVDLSKVTSKCGSLGNIHHKPGG GSVQIVYKPVDLSKVTSKCGSLGNIHHKPGGGSVQIVYKPVDLSKVTSKCGSLGNIHHKPGGGSVQIVYKPVDLSKVTSKCGSLG NIHHKPGGGSVQIVYKPVDLSKVTSKCGSLGNIHHKPGGGSVQIVYKPVDLSKVTSKCGSLGNIHHKPGGGSVQIVYKPVDLSKV TSKCGSLGNIHHKPGGGSVQIVYKPVDLSKVTSKCGSLGNIHHKPGGGSVQIVYKPVDLSKVTSKCGSLGNIHHKPGGGSVQIVY KPVDLSKVTSKCGSLGNIHHKPGGGSVQIVYKPVDLSKVTSKCGSLGNIHHKPGGGSVQIVYKPVDLSKVTSKCGSLGNIHHKPG GGSVQIVYKPVDLSKVTSKCGSLGNIHHKPGGGSVQIVYKPVDLSKVTSKCGSLGNIHHKPGGGSVQIVYKPVDLSKVTSKCGSL GNIHHKPGGGSVQIVYKPVDLSKVTSKCGSLGNIHHKPGGGSVQIVYKPVDLSKVTSKCGSLGNI".



# Protocol for MNPs/aptamer conjugation

**Samples:** Initial concentration 0.16 mg/mL in double distilled water of ( $\emptyset^{\sim}$  50 nm) Fe<sub>3</sub>O<sub>4</sub>/Au core/shell nanoparticles (AuFe18, AuFe25: 2 different batches of same synthesis route).

Step1:	Centrifuge Fe <sub>3</sub> O <sub>4</sub> /Au nanoparticles and redilute in ½ Volume (Final Concentration=0.32
	mg/mL)

Fe<sub>3</sub>O<sub>4</sub>/Au nanoparticles gentle mix

**Step2:** with 2  $\mu$ M (final concentration) of RNV95<sup>64</sup> or A $\beta$ 7-92-1H1<sup>65</sup>,

or with 1  $\mu$ M (final concentration) of TBA1<sup>66</sup>.

Step3: After 15 min, citrate-Na pH 3 (final concentration 10 mM) were added to reaction and samples were left for 15 min to rest.

**Step4:** Subsequently, MNPs-aptamer conjugates were frozen for 16 h (-20°C).

Step5: After thawing the samples in dark and room temperature, tubes were centrifuged for 15 min, 10,000 rpm, 4°C and washed three times with 10 mM Tris-EDTA buffer pH 8.

**Step6:** Finally, MNPs-aptamer conjugates were resuspended in TE and stored in dark.

The quantity of bound aptamer was determined with fluorescence (Excitation 490 nm, **Step7:** Emission 510-570 nm) at a Promega Glomax Multi-detection system using a fluorescence

standard calibration curve.

<sup>64</sup> RNV95 (5'-TGGGGGGCGGACGATAGGGGCCCCCCGGTAGGATGGACG-3') targeting low-molecular weight aggregates of Aβ40 amyloid (see Chakravarthy et al. 2018, <a href="https://doi.org/10.1039/C8CC02256A">https://doi.org/10.1039/C8CC02256A</a> Bound Aptamer: 0.15 μM

\_

<sup>65</sup> Aβ7-92-1H1 (5'-CGGTGGGGGACCAGTACAAAAGTGGGTAGGGCGGGTTGGAAAA-3') targeting low-molecular weight aggregates of Aβ42 amyloid (see Zheng et al. 2020, <a href="https://doi.org/10.1021/acsabm.0c00996">https://doi.org/10.1021/acsabm.0c00996</a> Bound Aptamer: ~0.22 μΜ

<sup>&</sup>lt;sup>66</sup> TBA1 (5'- GGTTGGTGGTTGG-3') targeting the fibrinogen-recognition exosite of thrombin (see Zheng et al. 2020, https://doi.org/10.1006/jmbi.1996.0097 Bound Aptamer:~0.22 μM



Supple Graphene Bio-Platform for point-of-care early detection and monitoring of Alzheimer's Disease























## Follow us



